

**Crustal Stress Studies
Using
Microearthquakes and Boreholes**

BY

BJÖRN LUND

UPPSALA UNIVERSITY 2000

Dissertation for the Degree of Doctor of Philosophy in Geophysics presented at Uppsala University in 2000

ABSTRACT

Lund, B. 2000. Crustal stress studies using microearthquakes and boreholes. Acta Universitatis Upsaliensis. *Comprehensive Summaries of Uppsala Dissertations from the Faculty of Science and Technology* 517. 75 pp. Uppsala. ISBN 91-554-4671-X.

The state of stress in the crust is essential for the understanding of geodynamic processes such as the transmission of plate driving forces through the lithosphere and the triggering of earthquakes. This thesis describes the development and application of new methods for the estimation of crustal stresses. The first study revisits the stress state of the Swedish upper crust using data from the deep boreholes in Siljan. The analysis of wellbore image and other logging data enables us to constrain orientations and magnitudes of *in situ* stress. We find a strike-slip faulting regime at depth with the maximum horizontal stress in a WNW–ESE direction and $S_H - S_h \sim 60$ MPa at 5 km depth. The remaining three studies in this thesis are concerned with stress estimation from microearthquakes. We utilize earthquake data from the Icelandic SIL network in southwest Iceland. The first microearthquake study develops a stress tensor inversion scheme for focal mechanisms, including new methods for the selection of fault plane from the nodal planes as well as a novel technique to account for the errors in the focal mechanisms. The second study introduces a new method to assess the similarity of focal mechanisms for earthquakes with closely located hypocenters. The method is also promising as a monitoring instrument of earthquake repeating patterns. Finally, these new methods are applied to one year of seismicity before the November 13, 1998, $M_L = 5.0$ Ölfus earthquake. During the year we find significant temporal variations in microearthquake repeating patterns, and a large anomaly ending at the main event. The estimated background state of stress is well constrained, stress inversions over time show a rather stable, subhorizontal direction of σ_3 with more variations in σ_1 and σ_2 .

Björn Lund, Department of Earth Sciences, Uppsala University, Villavägen 16, SE-752 36 Uppsala, Sweden

© Björn Lund 2000

ISSN 1104-232X

ISBN 91-554-4671-X

Printed in Sweden by Eklundshofs Grafiska AB, Uppsala 2000

List of papers

This thesis is based on the following papers, which will be referred to in the text by their Roman numerals I - IV.

- I. Orientation and magnitude of *in situ* stress to 6.5 km depth in the Baltic Shield.
B. Lund and M.D. Zoback, *Int. J. Rock. Mech. Min. Sci.*, **36**, 169-190, 1999.
- II. Stress tensor inversion using detailed microearthquake information and stability constraints: Application to Ölfus in southwest Iceland.
B. Lund and R. Slunga, *J. Geophys. Res.*, **104**, 14,947-14,964, 1999.
- III. Correlation of microearthquake body-wave spectral amplitudes.
B. Lund and R. Böðvarsson, submitted to *Bull. Seismol. Soc. Am.*, 1999.
- IV. Spectral amplitude grouping and the state of stress: A study of microearthquake activity before the November 13, 1998, magnitude 5.0 earthquake in Ölfus, Iceland.
B. Lund, R. Slunga and R. Böðvarsson, manuscript.

Papers written during my time at the Department of Earth Sciences but not included in this thesis:

- Comment on “Using borehole breakouts to constrain the complete stress tensor: Results from the Siljan Deep Drilling Project Project and offshore Santa Maria Basin, California” by Blair J. Zajac and Joann M. Stock.
B. Lund and C. Juhlin, *J. Geophys. Res.*, accepted 1999.
- Estimates of current Icelandic stress tensors from the inversion of micro-earthquake fault plane solutions.
B. Lund, R. Slunga and R. Böðvarsson, *GFF*, **118**, A95, 1996.

Reprints were made with kind permissions from Elsevier Science (I) and the American Geophysical Union (II).

Contents

A note on notation	6
1 Introduction	7
2 The Stress Tensor	8
2.1 Properties of the stress tensor	10
2.2 Stress on a fault plane	12
2.3 Stress around a borehole	14
2.4 Transformation to the principal stress coordinate system	16
2.5 Direction of horizontal stress	16
2.6 Visualizing the stress tensor: Stress ellipse and Mohr circle	18
2.7 Rock fracture, friction and pore pressure	20
3 Stress information from microearthquakes	23
3.1 The seismic moment tensor	24
3.2 P and T axes and the stress tensor	27
3.3 Determining fault orientations from seismic wave observations	29
3.4 Inverting focal mechanisms for the stress tensor	30
3.4.1 On the distribution of data	32
3.4.2 Magnitudes of the principal stresses	33
4 Stress information from deep boreholes	34
4.1 Hydraulic fracturing	34
4.2 Borehole breakouts	38
4.3 Drilling-induced tensile wall-fractures	41
5 Iceland and the SIL network	43
5.1 Brief introduction to the tectonics of Iceland	43
5.2 SIL: The Icelandic seismic network	45
6 Summary of papers	46
6.1 Paper I	46
6.2 Paper II	49
6.3 Paper III	53
6.4 Paper IV	58
7 Concluding reflexions	63
Acknowledgements	66
References	68

A Computer programs	73
A.1 sti	73
A.2 ampcorr	74

A note on notation

In this thesis I will attempt to stick to the following stress notation conventions. In the first sections σ_{ij} signifies any general stress tensor but once the concept of effective stress has been introduced σ_{ij} is the effective stress and S_{ij} the applied stress. All stresses are considered positive when compressive. The term *hydrostatic stress* is often used for the situation $\sigma_1 = \sigma_2 = \sigma_3$. This becomes a little confusing when pore pressures and boreholes are present and I will reserve hydrostatic for the stress (or pressure) exerted by the weight of a unit area column of the fluid in question. Vectors are in bold, \mathbf{n} , tensors and matrices bold underlined, $\underline{\mathbf{A}}$.

$\underline{\boldsymbol{\sigma}}, \underline{\mathbf{D}}, \underline{\mathbf{T}}$	General, deviatoric and reduced stress tensor
$\sigma_{xx}, \sigma_{yy}, \sigma_{zz},$ $\sigma_{11}, \sigma_{22}, \sigma_{33}$	Normal stress components in a Cartesian coordinate system
$\sigma_{rr}, \sigma_{\theta\theta}, \sigma_{zz},$	Normal stress components in a cylindrical coordinate system
$\sigma_{xy}, \sigma_{xz}, \sigma_{yz},$ $\sigma_{12}, \sigma_{13}, \sigma_{23}$	Shear stress components in a Cartesian coordinate system
$\sigma_{r\theta}, \sigma_{rz}, \sigma_{\theta z},$	Shear stress components in a cylindrical coordinate system
$\sigma_1, \sigma_2, \sigma_3$	Magnitudes of the principal stresses
$\boldsymbol{\sigma}_1, \boldsymbol{\sigma}_2, \boldsymbol{\sigma}_3$	Principal stress vectors
$\hat{\boldsymbol{\sigma}}_1, \hat{\boldsymbol{\sigma}}_2, \hat{\boldsymbol{\sigma}}_3$	Orthonormal basis vectors in the principal stress directions
$\sigma_{1N}, \sigma_{1E}, \sigma_{1d}$	Components of $\hat{\boldsymbol{\sigma}}_1$ in the North, East, down coord. sys.
\mathbf{n}	Vector normal to a plane, unit length
\mathbf{t}	Traction vector on a plane
$\sigma_n, \boldsymbol{\sigma}_n$	Normal stress magnitude and vector, on a plane
$\tau, \boldsymbol{\tau}$	Shear stress magnitude and vector, in a plane
$\sigma_H, \sigma_h, \sigma_V$	Maximum and minimum horizontal stress and vertical stress
P, P_0, P_b	General fluid pressure, pore pressure, borehole fluid pressure

1 Introduction

Despite our long traditions of using rock as a construction material, traditions probably as old as civilization itself, it was only during the last century that the need to understand and measure the forces acting in the rock became urgent. The foundation of tall buildings and long bridges, the excavation of long tunnels and deep mines and the drilling of deep wells can only be safely carried out with knowledge of how the rock responds to changes in the stress field. The advancement of civil, mining and petroleum engineering spurred interest in the measurement of rock stresses and from the relief methods of the 1930s the development of new stress measurement techniques has been constantly increasing. At the same time, in geology and geophysics, the need for quantitative estimates of the development of folds and intrusions, the movement of earthquake generating faults etc., accentuated the need for estimates of *in situ* stress from the deep crust. Further interest in deep stress estimates was triggered by the plate tectonic revolution. Plate tectonics has been very successful in describing various tectonic processes by a single concept, but the forces that drive the plates are still not well understood. Which forces act on the plates, where do they act, what are their magnitudes and how and where are they transmitted? Some of these questions can be answered through the study of mechanical stresses in the lithosphere. The recent interest in stress transfer and stress triggering of earthquakes is a field which requires detailed knowledge of crustal stresses, preferably both before and after large earthquakes. Accurate estimates of the background stress field and the perturbations caused by smaller groups of events will contribute to the understanding of earthquake generating mechanisms and, hopefully one day, the forecasting of earthquakes.

This thesis describes some new developments in the estimation of crustal stresses from earthquake focal mechanisms and a new method for the monitoring of one aspect of earthquake faulting, based on focal mechanisms and locations. An application of an integrated stress measurement strategy, utilizing two deep boreholes to measure crustal stress, is also included in the thesis.

The thesis is divided into two parts. The first part starts with an introduction to the stress tensor concept and to some of the properties and applications of the stress tensor. Included in this section is also a very brief summary of rock fracture, friction and pore pressure. In the next section I introduce the methods used to infer stress from earthquake focal mechanisms and include some comments on the use of P and T axes as stress orientation indicators. This section also contains a discussion on the distribution of focal mechanism data, pertaining to stress tensor inversion. The third major section of this part of the thesis describes some of the methods used for inferring stresses from deep boreholes. I have concentrated on hydraulic fracturing, borehole breakouts and induced tensile fracturing. Since all of the data for the seismological part of this thesis come from the Icelandic SIL network, I have included a very brief introduction to the tectonics of Iceland and

the operation of the SIL network. After SIL follows the summaries of the papers and a few concluding remarks.

The second, or main, part of the thesis consists of four papers. Paper I describes the estimation of the orientation and magnitude of the state of stress in Siljan, Sweden, using data from the deep boreholes Gravberg-1 and Stenberg-1. All stress related data obtained from the two boreholes have been compiled and analyzed using an integrated stress measurement strategy. Papers II, III and IV are all based on microearthquake data from Ölfus in southwest Iceland. Paper II extends an earlier stress inversion method by introducing a new nodal plane selection criterion, and through the use of acceptable focal mechanisms it allows for errors in the mechanisms. Paper III introduces a new technique for assessing the similarity of focal mechanisms, which is also discovered to be very valuable as a monitor of earthquake repeating patterns. In Paper IV we apply the methods developed in Paper II and III in a study of one year of seismicity prior to the November 13, 1998, magnitude 5.0 earthquake in Ölfus.

2 The Stress Tensor

Stress is defined by considering a force, $\partial\mathbf{F}$, acting on a surface, ∂A , see Figure 1A. The limiting value of $\mathbf{t} = \partial\mathbf{F}/\partial A$ as the surface ∂A goes to zero is called the traction vector, or sometimes the stress vector. Following *Jaeger and Cook* [1979] I use the sign convention that compressive stresses are positive. In order to completely describe the stresses acting at a point in an elastic medium, consider the stresses acting on the infinitesimally small cube of material in Figure 1B. Stress components acting perpendicular to the surfaces are called *normal* stresses and denoted

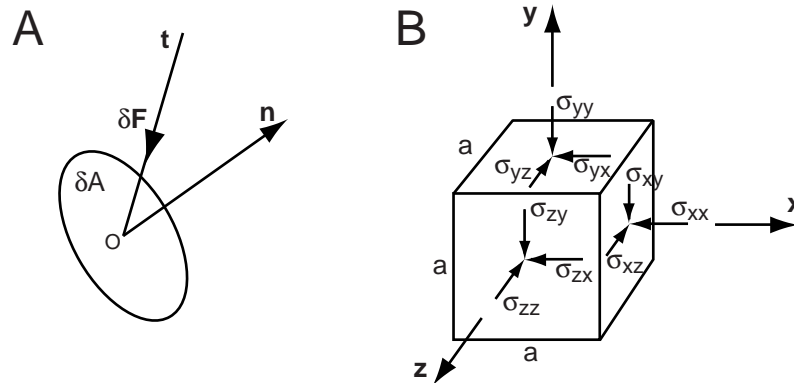


Figure 1: A) Definition of stress on a plane with area ∂A subject to a force $\partial\mathbf{F}$. Traction vector \mathbf{t} and plane normal \mathbf{n} . B) Infinitesimal material cube showing the nine components of the stress tensor. Compression is positive.

σ_{xx} , σ_{yy} and σ_{zz} . Stress components acting along planes are referred to as *shear* stresses and denoted σ_{xy} , σ_{xz} etc. I use the subscript notation *on-in*, i.e. the stress components act *on* the surface denoted by the first subscript *in* the direction denoted by the second subscript. Shear stresses are considered positive as indicated in Figure 1B. In the static case, when all forces acting on three orthogonal faces of a body are in equilibrium, we can write the nine stress components in a Cartesian coordinate system as

$$\begin{pmatrix} \sigma_{xx} & \sigma_{xy} & \sigma_{xz} \\ \sigma_{yx} & \sigma_{yy} & \sigma_{yz} \\ \sigma_{zx} & \sigma_{zy} & \sigma_{zz} \end{pmatrix} \quad (1)$$

Furthermore, inspecting Figure 1B we intuitively see that if σ_{xy} is not equal to σ_{yx} there would be a couple $a^3(\sigma_{xy} - \sigma_{yx})$, where a is the length of the side of the cube, acting to rotate the cube. For the angular moments on the cube to be in equilibrium, e.g. around the z -axis

$$2\sigma_{xy} + \frac{\partial\sigma_{xy}}{\partial x}a - 2\sigma_{yx} + \frac{\partial\sigma_{yx}}{\partial y}a = 0 \quad (2)$$

and as $a \rightarrow 0$, we require $\sigma_{xy} = \sigma_{yx}$, and similarly $\sigma_{xz} = \sigma_{zx}$ and $\sigma_{yz} = \sigma_{zy}$. The stress matrix is hence diagonally symmetric (for a more stringent proof see e.g. *Aki and Richards* [1980] p. 19), it is always real and only six of the nine components are independent. We know from matrix theory that real symmetric matrices have important properties such as real eigenvalues, orthogonal eigenvectors and that they are orthogonally diagonalizable.

At this point it is convenient to introduce the tensor concept. Intuitively, a tensor can be thought of as a quantity composed of a collection of vectors, and in three dimensions a tensor is a combination of three vectors. This is analogous to considering a vector a collection of scalars, which in three dimensions are three scalars. More rigorously, a tensor is a quantity that is defined only in terms of its transformation properties under orthogonal coordinate transformations [*Goldstein*, 1980]. In Cartesian three-dimensional space, a tensor $\underline{\mathbf{S}}$ of the N th rank may be defined as a quantity having 3^N components $S_{ijk\dots}$ (with N indices that run from 1 to 3) that transform under an orthogonal transformation $\underline{\mathbf{A}}$ as

$$S'_{ijk\dots}(\mathbf{x}') = a_{il}a_{jm}a_{kn}\dots S_{lmn\dots}(\mathbf{x}) \quad (3)$$

By this definition, a scalar is a tensor of rank zero and is invariant under orthogonal transformation. A first rank tensor has three components transforming as

$$S'_i = a_{ij}S_j \quad (4)$$

and is hence equivalent to a vector. The nine components of a second rank tensor transforms as

$$S'_{ij} = a_{ik}a_{jl}S_{kl} \quad (5)$$

which is precisely how our symmetric stress matrix transforms. Using matrix notation, Equation 5 can be written more compact as

$$\underline{\mathbf{S}}' = \underline{\mathbf{A}} \underline{\mathbf{S}} \underline{\mathbf{A}}^T \quad (6)$$

I will use Equation 6 extensively in later stress tensor coordinate transformations.

2.1 Properties of the stress tensor

During transformations of the stress tensor there are some quantities that do not change, that are *invariant*. These are, in addition to the eigenvalues, the coefficients of the characteristic equation that defines the eigenvalues.

$$\begin{vmatrix} \sigma_{xx} - \lambda & \sigma_{xy} & \sigma_{xz} \\ \sigma_{yx} & \sigma_{yy} - \lambda & \sigma_{yz} \\ \sigma_{zx} & \sigma_{zy} & \sigma_{zz} - \lambda \end{vmatrix} = 0 \quad (7)$$

giving the characteristic equation

$$\lambda^3 - \text{tr}(\sigma_{ij})\lambda^2 + \text{minor}(\sigma_{ij})\lambda - \det(\sigma_{ij}) = 0 \quad (8)$$

where

$$\text{tr}(\sigma_{ij}) = \sigma_{xx} + \sigma_{yy} + \sigma_{zz} \quad (9)$$

$$\text{minor}(\sigma_{ij}) = \sigma_{xx}\sigma_{yy} + \sigma_{yy}\sigma_{zz} + \sigma_{xx}\sigma_{zz} - \sigma_{yx}^2 - \sigma_{zy}^2 - \sigma_{zx}^2 \quad (10)$$

$$\det(\sigma_{ij}) = \sigma_{xx}\sigma_{yy}\sigma_{zz} + 2\sigma_{yx}\sigma_{zy}\sigma_{zx} - \sigma_{xx}\sigma_{zy}^2 - \sigma_{yy}\sigma_{zx}^2 - \sigma_{zz}\sigma_{yx}^2 \quad (11)$$

The trace (tr), the sum of minors and the determinant (det) of the stress tensor hence always stay constant during transformations and can be used to verify that transformation algorithms work properly. The invariants are also important in the formulation of failure criteria. The trace is related to the mean normal stress component of the stress field which is defined as $\mathcal{S} = \text{tr}(\sigma_{ij})/3$.

We noted above that real symmetric matrices have real eigenvalues, orthogonal eigenvectors and can be diagonalized. This implies that there always exists some coordinate system where the stress tensor is diagonal and this coordinate system is referred to as the *principal* system, where the shear stresses are zero on planes orthogonal to the coordinate axes and where the normal stresses act along the principal axes directions (the eigenvectors). The principal stress magnitudes (the eigenvalues) are denoted σ_1 , σ_2 and σ_3 and the stress tensor takes the simple form

$$\underline{\boldsymbol{\sigma}} = \begin{pmatrix} \sigma_1 & 0 & 0 \\ 0 & \sigma_2 & 0 \\ 0 & 0 & \sigma_3 \end{pmatrix} \quad (12)$$

where, by definition, $\sigma_1 \geq \sigma_2 \geq \sigma_3$. The principal stress system is very important in applications of stress theory to geophysics and geology. Calculations are usually

much simpler to perform in the principal system, as we shall see below, and when discussing crustal states of stress, faulting regimes and laboratory experiments, the principal stresses are frequently used. Due to the presence of the free surface, the stress field close to the Earth's surface is expected to have one principal stress vertical and hence two horizontal principal stresses. Numerous measurements from all over the world, using a wide variety of measurement techniques, indicate that this assumption is valid in most cases. One principal stress is commonly found to be inclined less than 30° to the vertical [Zoback *et al.*, 1989; Amadei and Stephansson, 1997]. These measurements also indicate that the magnitude of the vertical stress is commonly explained by the weight of the overburden [Amadei and Stephansson, 1997], i.e. $\sigma_V = \int_0^D \rho(z)g(z) dz$, where $\rho(z)$ is the density of the overlying rock, $g(z)$ gravity and D the depth. However, localized anomalies exist and have been attributed to local geological features or active tectonic zones [Amadei and Stephansson, 1997]. A state of stress in the crust where all principal stress magnitudes are equal to σ_V is often referred to as *lithostatic*. Contrary to the straightforward calculation of the vertical stress, the magnitudes of the horizontal stresses are much more difficult to predict. In some circumstances lithostatic stress conditions are assumed, another frequently used expression is $\sigma_V \nu / (1 - \nu)$, where ν is Poisson's ratio for the rock. This expression assumes (1) an ideal, homogeneous, linearly isotropic continuous half-space with horizontal surface, (2) a rock mass under gravity loading alone with vanishing horizontal displacements and (3) no influence of the loading history on the stress build up. In general, however, measurements show that horizontal stresses vary considerably and these variations are inferred to be caused by such diverse mechanisms as tectonic stress, thermal stress, erosion, anisotropy, glaciation and deglaciation, topography and other active geological features [Amadei and Stephansson, 1997].

It is sometimes convenient to subtract the mean normal stress component from the stress tensor and the resulting quantity is then called the *deviatoric* stress tensor, $\underline{D} = \underline{\sigma} - \mathcal{S}\underline{I}$. This separates the stress tensor into one component that determines the uniform compression or dilatation, and one component that determines the distortion or shearing, the deviatoric component. The deviatoric stress is important in failure criteria since these are primarily concerned with shearing stresses. $\sigma_1 - \sigma_3$ is sometimes referred to as the magnitude of the deviatoric stress.

Another method of decomposing the stress tensor was suggested by Angelier *et al.* [1982], which I follow using a measure of the relative size of the intermediate principal stress $R = (\sigma_1 - \sigma_2) / (\sigma_1 - \sigma_3)$ after Gephart and Forsyth [1984], where $0 \leq R \leq 1$.

$$\underline{\sigma} = \begin{pmatrix} \sigma_1 - \sigma_3 & 0 & 0 \\ 0 & \sigma_2 - \sigma_3 & 0 \\ 0 & 0 & \sigma_3 - \sigma_3 \end{pmatrix} + \sigma_3 \underline{I} \quad (13)$$

$$\underline{\sigma} = (\sigma_1 - \sigma_3) \begin{pmatrix} 1 & 0 & 0 \\ 0 & 1 - R & 0 \\ 0 & 0 & 0 \end{pmatrix} + \sigma_3 \underline{\mathbf{I}} \quad (14)$$

$$\underline{\sigma} = (\sigma_1 - \sigma_3) \underline{\mathbf{T}} + \sigma_3 \underline{\mathbf{I}} \quad (15)$$

We see that the stress tensor is decomposed into a *reduced* stress tensor, $\underline{\mathbf{T}}$, multiplied with a constant that is a measure of the shear stress magnitude, plus an isotropic component. The choice of R might seem odd in this context, *Angelier et al.* [1982] instead used the more natural choice $\phi = (\sigma_2 - \sigma_3)/(\sigma_1 - \sigma_3) = 1 - R$, but we shall see below that R is useful when resolving the shear stress on a plane.

2.2 Stress on a fault plane

Consider a fault plane with normal $\mathbf{n} = (n_1, n_2, n_3)$ in a homogeneous stress field $\underline{\sigma}$ as in Figure 2. Performing all calculations in the principal stress system we can easily obtain the components of the normal, σ_n , and shear, τ , stresses. The traction vector \mathbf{t} is given by

$$-\mathbf{t} = \underline{\sigma} \mathbf{n} = (\sigma_1 n_1, \sigma_2 n_2, \sigma_3 n_3) \quad (16)$$

remembering that our sign convention dictates that compressive stress is positive and thus has the opposite direction to the plane normal. From the traction vector we calculate the normal and shear stresses on the plane

$$-\sigma_n = (\mathbf{t} \cdot \mathbf{n}) \mathbf{n} = (\sigma_1 n_1^2 + \sigma_2 n_2^2 + \sigma_3 n_3^2) \mathbf{n} \quad (17)$$

$$-\boldsymbol{\tau} = \mathbf{t} - \sigma_n \quad (18)$$

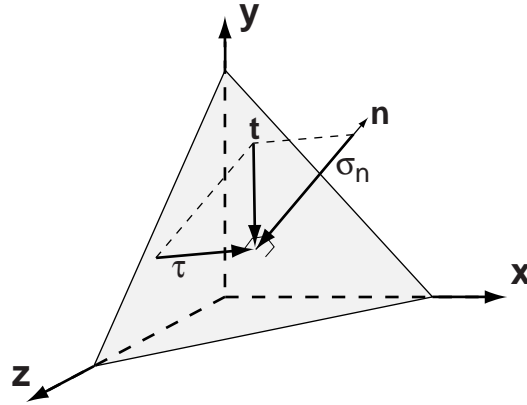


Figure 2: Decomposition of the traction vector \mathbf{t} on a plane into the normal stress σ_n and shear stress τ components.

We find for the shear stress components

$$\begin{aligned} -\tau_1 &= (\sigma_1 - (\sigma_1 n_1^2 + \sigma_2 n_2^2 + \sigma_3 n_3^2))n_1 \\ -\tau_2 &= (\sigma_2 - (\sigma_1 n_1^2 + \sigma_2 n_2^2 + \sigma_3 n_3^2))n_2 \\ -\tau_3 &= (\sigma_3 - (\sigma_1 n_1^2 + \sigma_2 n_2^2 + \sigma_3 n_3^2))n_3 \end{aligned}$$

and using the relation $n_1^2 + n_2^2 + n_3^2 = 1$

$$\begin{aligned} -\tau_1 &= (n_2^2(\sigma_1 - \sigma_2) + n_3^2(\sigma_1 - \sigma_3))n_1 \\ -\tau_2 &= (n_2^2(\sigma_1 - \sigma_2) + n_3^2(\sigma_1 - \sigma_3) - (\sigma_1 - \sigma_2))n_2 \\ -\tau_3 &= (n_2^2(\sigma_1 - \sigma_2) + n_3^2(\sigma_1 - \sigma_3) - (\sigma_1 - \sigma_3))n_3 \end{aligned}$$

Finally, remembering that $R = (\sigma_1 - \sigma_2)/(\sigma_1 - \sigma_3)$ and using $K = n_3^2 + Rn_2^2$ we can write

$$-\boldsymbol{\tau} = (\sigma_1 - \sigma_3) \begin{pmatrix} Kn_1 \\ (K - R)n_2 \\ (K - 1)n_3 \end{pmatrix} \quad (19)$$

and hence the magnitude of the shear stress is

$$\tau = (\sigma_1 - \sigma_3) \sqrt{n_3^2 + R^2 n_2^2 - K^2} \quad (20)$$

Equation 19 shows that the direction of shear stress on a plane is independent of the absolute magnitude of the principal stresses and only depends on the orientation of the plane in the stress field and on the ratio R [Bott, 1959]. Comparing Equation 19 with Equation 15 we see that the shear stress direction on a fault plane is determined by the reduced stress tensor and that neither adding an isotropic stress nor multiplying the tensor with a positive constant will modify that direction. This result is central to inversion schemes that estimate the principal stresses from earthquake focal mechanisms.

The maximum shear stress directions and magnitudes are obtained from the stationary points when Equation 20 is differentiated with respect to the coordinates of the fault plane. I will only state the results here, for a full treatment see e.g. *Jaeger and Cook* [1979]. There are three directions of maximum shear stress, all of which bisect the angles between the principal stresses. The greatest is

$$\tau = \frac{1}{2}(\sigma_1 - \sigma_3) \quad (21)$$

bisecting the directions of σ_1 and σ_3 . The other stationary values are, as expected,

$$\tau = \frac{1}{2}(\sigma_1 - \sigma_2) \quad \tau = \frac{1}{2}(\sigma_2 - \sigma_3) \quad (22)$$

The normal stresses corresponding to these directions are

$$\frac{1}{2}(\sigma_1 + \sigma_3) \quad \frac{1}{2}(\sigma_1 + \sigma_2) \quad \frac{1}{2}(\sigma_2 + \sigma_3) \quad (23)$$

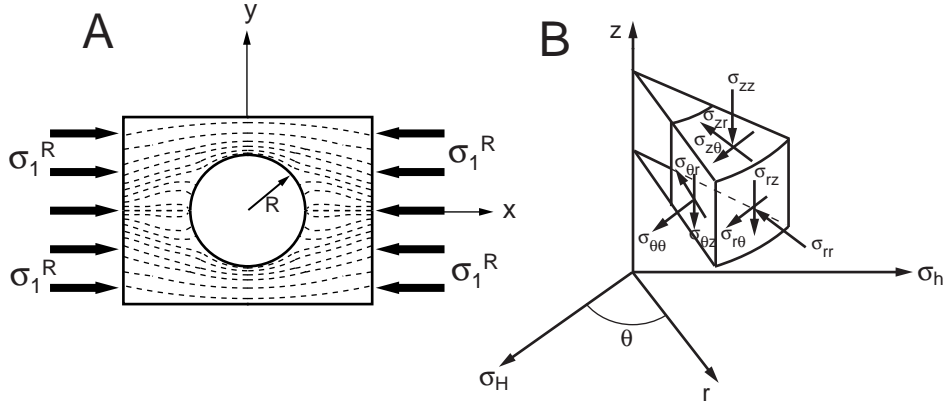


Figure 3: A) Circular hole in a material under uniaxial, compressive stress of magnitude σ_1^R at infinity. B) Coordinate system and orientations of the components of the stress tensor in cylindrical coordinates.

2.3 Stress around a borehole

If a circular hole is made in a homogeneous body experiencing a homogeneous stress field, stress will concentrate around the hole since no force can be carried through the interior void. Figure 3A shows the stress concentration around the hole in a body under uniaxial compression, of magnitude σ_1^R in the far-field, in the x -direction. Since the hole boundary is a free surface, the stresses acting normal to the boundary must decrease to zero at the boundary. As I will show below, at the point $x = 0$, $y = \pm R$, we have the largest compressive stress, $\sigma_{xx} = 3\sigma_1^R$ and $\sigma_{yy} = 0$. At $x = \pm R$ and $y = 0$, we have the largest tensile stress, $\sigma_{xx} = 0$ and $\sigma_{yy} = -\sigma_1^R$. Even if the hole is filled with other material, of differing elastic moduli, there would be a perturbation in the stress field around the inclusion. The equations governing the stresses around a hole are best represented in polar coordinates, for the 3D case cylindrical coordinates will be used, see Figure 3B. The stress equations are obtained by considering the equilibrium equations in the three coordinate directions, e.g. in the case of the tangential (or hoop) stress, $\sigma_{\theta\theta}$, we require the tangential forces to sum to zero, $\sum F_\theta = 0$, which yields

$$\frac{1}{r} \frac{\partial \sigma_{\theta\theta}}{\partial \theta} + \frac{\partial \sigma_{r\theta}}{\partial r} + \frac{2}{r} (\sigma_{r\theta}) = 0 \quad (24)$$

If we assume that the rock is elastic and isotropic and that the borehole is parallel to one of the principal stresses, an example is a vertical borehole in an area where the vertical stress, σ_V , is a principal stress, we obtain the analytical solutions

described already by *Kirsch* [1898].

$$\begin{aligned}\sigma_{rr} &= \frac{1}{2}(\sigma_H + \sigma_h) \left(1 - \frac{R^2}{r^2}\right) + \frac{1}{2}(\sigma_H - \sigma_h) \left(1 - 4\frac{R^2}{r^2} + 3\frac{R^4}{r^4}\right) \cos 2\theta + \frac{\Delta P R^2}{r^2} \\ \sigma_{\theta\theta} &= \frac{1}{2}(\sigma_H + \sigma_h) \left(1 + \frac{R^2}{r^2}\right) - \frac{1}{2}(\sigma_H - \sigma_h) \left(1 + 3\frac{R^4}{r^4}\right) \cos 2\theta - \frac{\Delta P R^2}{r^2} \\ \sigma_{r\theta} &= -\frac{1}{2}(\sigma_H + \sigma_h) \left(1 + 2\frac{R^2}{r^2} - 3\frac{R^4}{r^4}\right) \sin 2\theta\end{aligned}$$

σ_H and σ_h are the maximum and minimum horizontal stresses, θ is the angle around the borehole from the direction of the maximum horizontal stress, see Figure 3B, R is the borehole radius and r the radial distance to the point of measurement ($r \geq R$) and ΔP is the difference between the fluid pressure in the borehole, P_b , and the formation pore pressure, P_0 . At the borehole wall, $r = R$, the equations simplify to

$$\sigma_{rr} = \Delta P \quad (25)$$

$$\sigma_{\theta\theta} = \sigma_H + \sigma_h - 2(\sigma_H - \sigma_h) \cos 2\theta - \Delta P \quad (26)$$

$$\sigma_{r\theta} = 0 \quad (27)$$

Comparing these equations with the simple case considered in Figure 3A, we see that the equations further simplify to the results stated above, at $\theta = 0$ and $\theta = 90^\circ$ with $\sigma_H = \sigma_1$, $\sigma_h = 0$ and $\Delta P = 0$.

The general case with a borehole arbitrarily inclined in the stress field was considered by *Hiramatsu and Oka* [1962] and *Fairhurst* [1968], here I will only state the equations evaluated at the borehole wall, $r = R$. The stresses referred to below, σ_{ij} $i, j = 1, 2, 3$, are stresses in a borehole local Cartesian coordinate system where the z-axis lies along the borehole axis, the x-axis is in the plane perpendicular to the borehole axis directed towards the bottom side of the borehole and the y-axis is in the same plane but perpendicular to x. This is the coordinate system utilized by *Peška and Zoback* [1995]. The cylindrical coordinate system is also local to the borehole with the z-axis parallel to the borehole axis.

$$\begin{aligned}\sigma_{rr} &= \Delta P \\ \sigma_{\theta\theta} &= \sigma_{11} + \sigma_{22} - 2(\sigma_{11} - \sigma_{22}) \cos 2\theta - 4\nu\sigma_{12} \sin 2\theta - \Delta P \\ \sigma_{zz} &= \sigma_{33} - 2\nu(\sigma_{11} - \sigma_{22}) \cos 2\theta - 4\nu\sigma_{12} \sin 2\theta \\ \sigma_{\theta z} &= 2(\sigma_{23} \cos \theta - \sigma_{13} \sin \theta)\end{aligned} \quad (28)$$

In this Cartesian coordinate system, θ is the angle from the x-axis around the borehole wall towards the y-axis. ν is Poisson's ratio. These general equations will be used for the borehole stress analysis in Paper I.

2.4 Transformation to the principal stress coordinate system

We have seen above that calculations of normal and shear stresses on a plane and stresses in a borehole are simple in the principal stress coordinate system. It is therefore advantageous to transform fault plane normals and borehole coordinates to the principal system before carrying out the calculations. We shall also see that the transformation of a vector from the geographic North, East, down (NEd) coordinate system, \mathbf{n}^{NEd} , to the principal stress system, \mathbf{n}^P , is very simple in the case where the principal stress axes are represented in NEd coordinates. We write the transformation

$$\mathbf{n}^P = \underline{\mathbf{A}}\mathbf{n}^{NEd} = \begin{pmatrix} \hat{\boldsymbol{\sigma}}_1 \cdot \mathbf{N} & \hat{\boldsymbol{\sigma}}_1 \cdot \mathbf{E} & \hat{\boldsymbol{\sigma}}_1 \cdot \mathbf{d} \\ \hat{\boldsymbol{\sigma}}_2 \cdot \mathbf{N} & \hat{\boldsymbol{\sigma}}_2 \cdot \mathbf{E} & \hat{\boldsymbol{\sigma}}_2 \cdot \mathbf{d} \\ \hat{\boldsymbol{\sigma}}_3 \cdot \mathbf{N} & \hat{\boldsymbol{\sigma}}_3 \cdot \mathbf{E} & \hat{\boldsymbol{\sigma}}_3 \cdot \mathbf{d} \end{pmatrix} \mathbf{n}^{NEd} \quad (29)$$

where $\hat{\boldsymbol{\sigma}}_i$ are unit vectors in the principal stress directions, in the NEd coordinate system, and $\mathbf{N} = (1, 0, 0)$, $\mathbf{E} = (0, 1, 0)$ and $\mathbf{d} = (0, 0, 1)$ are the basis vectors in the NEd system. Writing σ_{iN} , σ_{iE} and σ_{id} for the three components of $\hat{\boldsymbol{\sigma}}_i$, Equation 29 simplifies to

$$\mathbf{n}^P = \begin{pmatrix} \sigma_{1N} & \sigma_{1E} & \sigma_{1d} \\ \sigma_{2N} & \sigma_{2E} & \sigma_{2d} \\ \sigma_{3N} & \sigma_{3E} & \sigma_{3d} \end{pmatrix} \mathbf{n}^{NEd} = \begin{pmatrix} \hat{\boldsymbol{\sigma}}_1 \cdot \mathbf{n}^{NEd} \\ \hat{\boldsymbol{\sigma}}_2 \cdot \mathbf{n}^{NEd} \\ \hat{\boldsymbol{\sigma}}_3 \cdot \mathbf{n}^{NEd} \end{pmatrix} \quad (30)$$

Naturally, transforming vectors from the principal system to the NEd system is just as easy, we simply use the transpose of the transformation matrix above. This transformation matrix will be frequently used in the stress tensor inversion scheme for earthquake focal mechanisms described below. The stress tensor is there known in the principal system and we need to transform the planes of the earthquake focal mechanisms to the principal system.

2.5 Direction of horizontal stress

Using the results of the previous sections we can calculate the directions of the maximum and minimum horizontal stresses. Realizing that the horizontal stress equals the normal stress on a vertical plane, we define the normal of a horizontal plane as in Figure 4A, $\mathbf{n} = (n_N, n_E, 0) = (\cos \alpha, \sin \alpha, 0)$ in the NEd coordinate system. Using Equation 30 we find the plane normal in the principal stress system

$$\mathbf{n}^P = \begin{pmatrix} \sigma_{1N}n_N + \sigma_{1E}n_E \\ \sigma_{2N}n_N + \sigma_{2E}n_E \\ \sigma_{3N}n_N + \sigma_{3E}n_E \end{pmatrix} \quad (31)$$

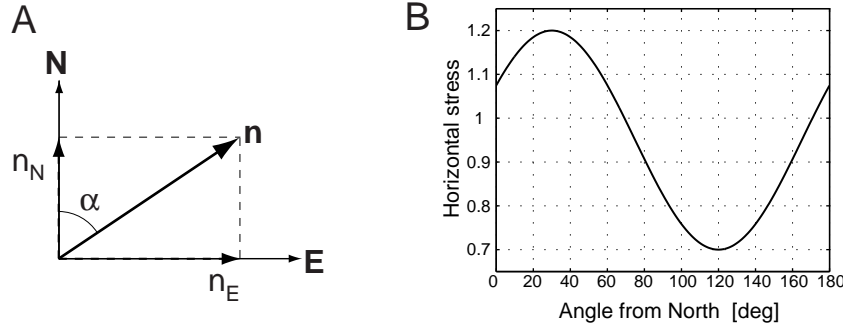


Figure 4: A) Vertical plane normal for the calculation of horizontal stress. B) Variation of σ_n with respect to the angle α . The direction of the principal stresses are σ_1 N30°E horizontal, σ_2 vertical, σ_3 N120°E horizontal and the magnitudes $\sigma_1 = 1.2$, $\sigma_2 = 1$, $\sigma_3 = 0.7$.

and Equation 17 gives us the plane normal, or horizontal, stress component

$$-\sigma_n = [\sigma_1(\sigma_{1N}n_N + \sigma_{1E}n_E)^2 + \sigma_2(\sigma_{2N}n_N + \sigma_{2E}n_E)^2 + \sigma_3(\sigma_{3N}n_N + \sigma_{3E}n_E)^2] \mathbf{n}^P \quad (32)$$

We find the stationary points, where σ_n has its maximum or minimum, by differentiating the magnitude of σ_n with respect to α

$$\frac{d|\sigma_n|}{d\alpha} = \sin 2\alpha[\sigma_1(\sigma_{1E}^2 - \sigma_{1N}^2) + \sigma_2(\sigma_{2E}^2 - \sigma_{2N}^2) + \sigma_3(\sigma_{3E}^2 - \sigma_{3N}^2)] + 2 \cos 2\alpha[\sigma_1\sigma_{1N}\sigma_{1E} + \sigma_2\sigma_{2N}\sigma_{2E} + \sigma_3\sigma_{3N}\sigma_{3E}] = 0 \quad (33)$$

σ_n will have one maximum and one minimum in the interval $0^\circ \leq \alpha \leq 180^\circ$, see Figure 4B for an example, and reorganizing Equation 33 we find

$$\tan 2\alpha = \frac{2(\sigma_1\sigma_{1N}\sigma_{1E} + \sigma_2\sigma_{2N}\sigma_{2E} + \sigma_3\sigma_{3N}\sigma_{3E})}{\sigma_1(\sigma_{1N}^2 - \sigma_{1E}^2) + \sigma_2(\sigma_{2N}^2 - \sigma_{2E}^2) + \sigma_3(\sigma_{3N}^2 - \sigma_{3E}^2)} \quad (34)$$

from which α can be determined. A test needs to be carried out, using the horizontal stress magnitude from Equation 32, to identify whether we found a maximum or minimum, and then the direction of the second horizontal stress, maximum or minimum, can be computed since we know that they are orthogonal to each other. Equation 34 fails (the denominator is zero) if we have one vertical principal stress and two horizontal principal stresses of equal magnitude. In such a case all horizontal stresses are equal. If $|\sigma_{1N}| = |\sigma_{1E}|$, $|\sigma_{2N}| = |\sigma_{2E}|$ and $|\sigma_{3N}| = |\sigma_{3E}|$ Equation 34 also fails, in this case the horizontal stresses have directions N45°E and N135°E, respectively.

Equation 34 seems to indicate that we need to know the magnitudes of the stresses to infer the direction of the maximum horizontal stress. This is, however,

not the case as we can see by considering the reduced stress tensor of Equation 15. The isotropic component of the stress tensor does not have any preferred direction and the $(\sigma_1 - \sigma_3)$ constant only affects the magnitude of the horizontal stress, i.e. the direction is only dependent on the reduced stress tensor. Starting again from the vertical plane normal in Equation 31 we now find the horizontal stress

$$-\boldsymbol{\sigma}_n = (\sigma_1 - \sigma_3) [(\sigma_{1N}n_N + \sigma_{1E}n_E)^2 + (1 - R)(\sigma_{2N}n_N + \sigma_{2E}n_E)^2] \mathbf{n}^P \quad (35)$$

and hence the expression for the angle is

$$\tan 2\alpha = \frac{2(\sigma_{1N}\sigma_{1E} + (1 - R)\sigma_{2N}\sigma_{2E})}{(\sigma_{1N}^2 - \sigma_{1E}^2) + (1 - R)(\sigma_{2N}^2 - \sigma_{2E}^2)} \quad (36)$$

As described above we need to test the solution by calculating the horizontal stress magnitudes. This is done using Equation 35, and since we are only interested in the relative sizes of the maximum and minimum horizontal stresses, we can neglect the unknown $(\sigma_1 - \sigma_3)$. The horizontal stress direction calculation using R fails in the same circumstances as did Equation 34. Being able to calculate the direction of maximum horizontal stress without knowledge of the principal stress magnitudes is very useful for visualizing the results of the stress tensor inversions described in Section 3.4, where no absolute magnitudes are retrieved.

2.6 Visualizing the stress tensor: Stress ellipse and Mohr circle

Adopting the principal stress axes as our reference system we know from Equation 16 that the traction vector on any plane with normal \mathbf{n} is

$$-\mathbf{t} = (\sigma_1 n_1, \sigma_2 n_2, \sigma_3 n_3)$$

Since all normals are assumed to have unit length, i.e. $n_1^2 + n_2^2 + n_3^2 = 1$, it follows that the components of the traction vector lie on an ellipsoid with semi-axes σ_1 , σ_2 and σ_3

$$\frac{t_x^2}{\sigma_1^2} + \frac{t_y^2}{\sigma_2^2} + \frac{t_z^2}{\sigma_3^2} = 1 \quad (37)$$

The *stress ellipsoid*, see Figure 5 left column, is a convenient tool to easily visualize the orientations and magnitudes of the principal stresses and hence the prevalent faulting regime and the magnitude of the shearing stresses.

The stress ellipsoid is, however, less convenient for showing the relationship between the orientation of a plane in the stress field and the resulting magnitudes of the normal and shear stresses upon it. To this respect we use the *Mohr circle* diagram which, as we shall see, is very useful also in the discussion of rock failure. I will not derive the angular relations for the Mohr circle here, see e.g. *Jaeger and Cook* [1979], instead the relationship between the normal to a fault plane and the

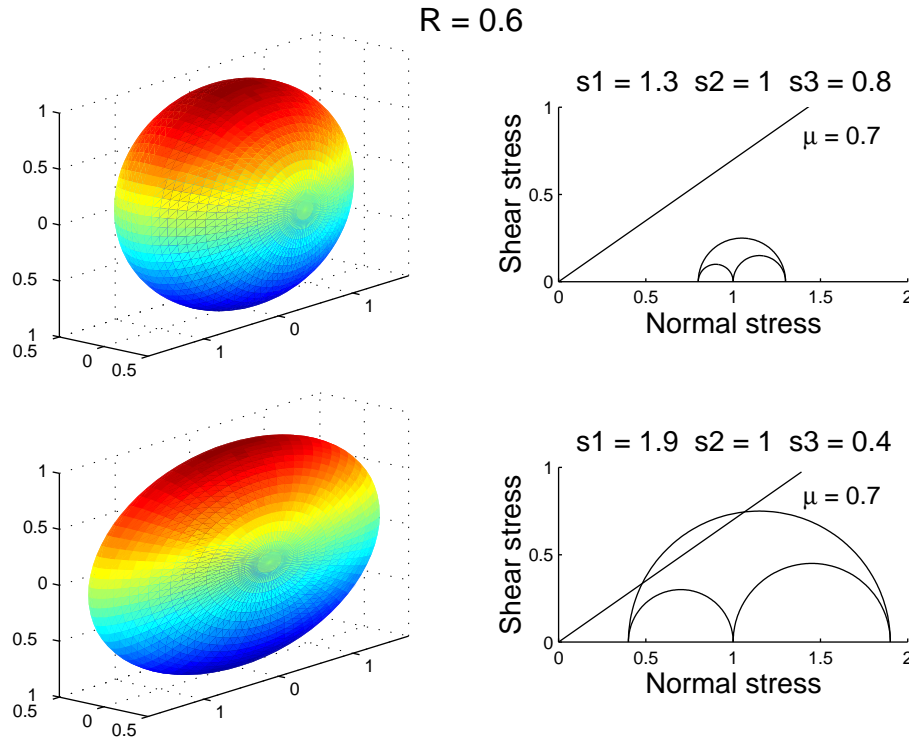


Figure 5: Stress ellipsoids and Mohr circles for two stress tensors with equal value of $R = 0.6$. The upper tensor has $\sigma_1 = 1.3$, $\sigma_2 = 1$ and $\sigma_3 = 0.8$ and the lower tensor has $\sigma_1 = 1.9$, $\sigma_2 = 1$ and $\sigma_3 = 0.4$. Observe the difference in the shapes of the stress ellipsoids but the identical shapes (except for a scale factor) of the Mohr circle diagrams.

normal, shear and principal stresses are illustrated in Figure 6. The angle between the σ_1 axis and the normal is denoted α and the angle between the σ_3 axis and the normal is θ . Using the equations for the magnitudes of the normal and shear stresses, Equations 17 and 20, we find that if one angle is kept fixed, varying the other angle traces out a circle in σ_n, τ space. If we fix one angle in the plane of two principal stresses, the three main circles in Figure 6B will be traced out, e.g. for a fault normal in the $\sigma_1 - \sigma_2$ plane ($\theta = 90^\circ$), Figure 6A, we have a circle centered on A (normal stress $(\sigma_1 + \sigma_2)/2$) in Figure 6B, with radius $(\sigma_1 - \sigma_2)/2$. We see from Figure 6B that normal stress for the circle varies from σ_1 to σ_2 and shear stress from 0 to $(\sigma_1 - \sigma_2)/2$, as we expect. Setting θ to any other angle will trace out other circles centered on A, such as the DEF circle segment. The largest of the three main circles traces out the stress magnitudes on normals in the $\sigma_1 - \sigma_3$ plane. If desired, the Mohr circles can be mirrored in the σ_n axis to allow for negative shear stress magnitudes. The space enclosed between the two

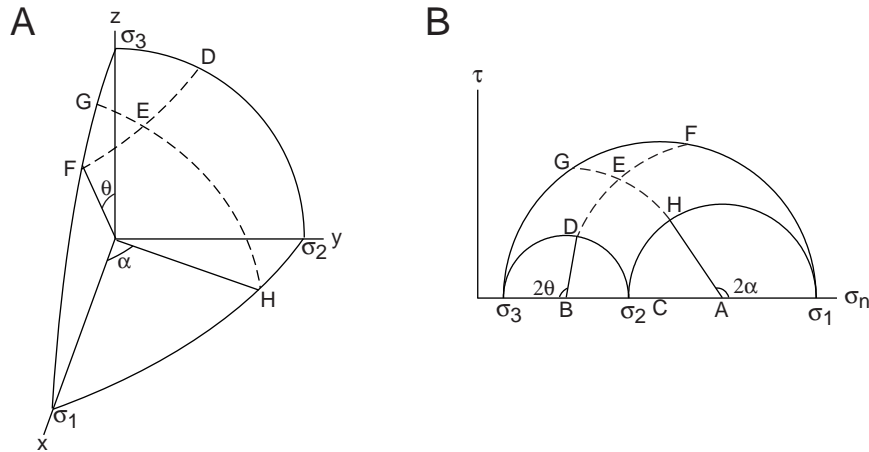


Figure 6: Figure modified after *Jaeger and Cook* [1979]. A) One octant of the stress ellipsoid showing the definitions of the angles α and θ and the traces of two ellipses for fixed values of α (GEH) and θ (DEF). B) The Mohr diagram corresponding to the stress ellipsoid in A.

smaller circles and the larger circle shows the possible shear and normal stresses on any plane in the stress field. Using the Mohr diagram we can hence read off the normal and shear stress magnitudes for any value of α and θ , i.e. any direction of the fault plane normal.

Comparing the stress ellipsoids and the Mohr diagrams in Figure 5 we see that although the ratio R is often referred to as the shape factor it does not describe the shape of the stress ellipsoid but instead the position of the σ_2 point in the Mohr diagram. R reflects how close σ_2 is to σ_1 or σ_3 , but it does not give any information on the magnitude of $(\sigma_1 - \sigma_3)$, i.e. the size of the Mohr diagram. An unscaled Mohr diagram can be constructed using only the directions of the principal stresses and R . Although without information on the absolute magnitude of the shear stress, such a diagram is valuable for the analysis of the relative stability of fault planes, since the location of the fault plane normal in the Mohr diagram only depends on the relative orientation of the fault plane normal with respect to the principal stress axes.

2.7 Rock fracture, friction and pore pressure

A material is said to be *brittle* under conditions in which its ability to resist load decreases with increasing deformation [*Jaeger and Cook*, 1979]. These conditions, such as low temperature and pressure, prevail for silicate rock in the Earth's upper lithosphere, which is consequently considered to be in a brittle state. Since most of this thesis will discuss only brittle material, this section will focus on brittle

failure.

The *strength* of a material can, in simplest terms, be viewed as the maximum stress that the material can support under given conditions. Theoretical calculations of strength often over-estimate the strength by orders of magnitude if they do not incorporate mechanisms to account for material defects such as cracks. To propagate the defects in the material, the theoretical strength has to be overcome only locally, within a stress concentration produced by the defect, hence the effective strength of the material is lowered. After failure has been initiated a complete loss of cohesion across a crack usually occurs, an effect called brittle *fracture*. To predict the onset of failure there exists a number of different failure criteria of which I will concentrate on the important Coulomb criterion.

Due to the difficulties in predicting rock failure mechanisms theoretically, the strength of rock under general stress conditions is described by empirical or semiempirical criteria. These criteria all relate the principal stresses, with some material parameters, so that they define a limiting failure envelope of the form [Scholz, 1990]

$$\sigma_1 = f(\sigma_2, \sigma_3) \quad (38)$$

For tensile failure the simple, but adequate, assumption that the material fails on a plane perpendicular to the least principal stress, σ_3 , when that stress falls below the uniaxial tensile strength T , results in the failure criterion

$$\sigma_3 = -T_0 \quad (39)$$

Shear failure under compressive stress is commonly described by the criterion introduced by *Coulomb* [1773] where shear failure is resisted by the cohesion, or intrinsic shear strength, of the material, τ_0 and by a constant times the normal stress across the plane

$$\tau = \mu\sigma_n + \tau_0 \quad (40)$$

where τ is the shear stress at failure and σ_n the normal stress on the plane. The parameter μ is called the *coefficient of internal friction*, in analogy with the coefficient of sliding friction for cohesionless soils. Stretching the analogy further we write $\tan\phi = \mu$ and refer to ϕ as the *angle of internal friction* after the steepest angle of repose for soils. Note, however, that the Coulomb criterion is strictly empirical.

The Mohr circle diagram is very useful in analyzing the Coulomb criterion since it is stated in terms of shear and normal stresses. In Figure 7A I have superimposed the failure line, **f1**, of Equation 40 on a Mohr circle of σ_1 and σ_3 . The slope of the failure line depends on the coefficient of friction, the larger the friction, the steeper the line. The Coulomb criterion is two-dimensional, there is no predicted effect of an intermediate stress, which is why I use the maximum and minimum principal stresses. If the $(\sigma_1 - \sigma_3)$ difference would have been large enough for the stress

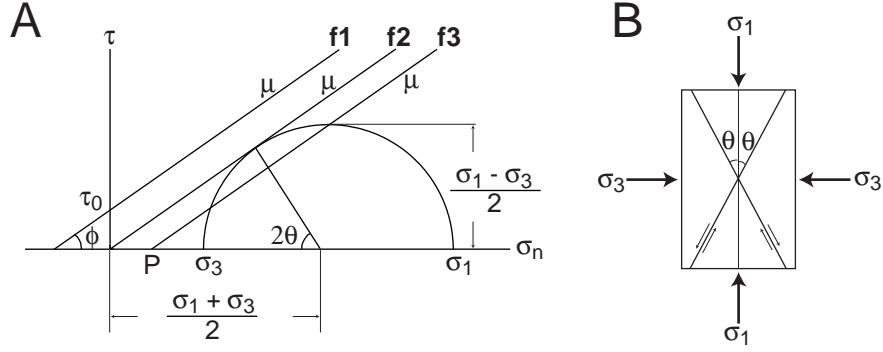


Figure 7: Figure modified after *Scholz* [1990]. A) Mohr circle for σ_1 and σ_3 illustrating the failure lines superimposed by the Coulomb criterion. B) Angular relationship between principal stresses and the fracture planes.

circle to reach the failure line **f1**, failure would occur and we see from the Mohr diagram that it would occur on two *conjugate* planes oriented at acute angles

$$\theta = \frac{\pi}{4} - \frac{\phi}{2} \quad (41)$$

on either side of the σ_1 axis and with opposite sense of shear direction, see also Figure 7B. Using Equation 17 and 20 for the normal and shear stress magnitudes and the geometry of Figure 7, we can describe the Coulomb criterion in terms of the principal stresses

$$\sigma_1 \left[\sqrt{\mu^2 + 1} - \mu \right] - \sigma_3 \left[\sqrt{\mu^2 + 1} + \mu \right] = 2\tau_0 \quad (42)$$

This is a straight line in the σ_1, σ_3 plane with intercept at the uniaxial compressive strength

$$C_0 = 2\tau_0 \left[\sqrt{\mu^2 + 1} + \mu \right] \quad (43)$$

on the σ_1 axis. Experiments using triaxial stress condition show generally good agreement with the Coulomb criterion [*Jaeger and Cook, 1979*] in that the σ_1 versus σ_3 curve is approximately linear and the shear fracture plane is inclined at an angle of less than 45° to the σ_1 direction.

Byerlee [1978] compiled measurements of frictional strength for a wide variety of rocks under different loads, and was able to fit the data with two straight lines. For lower normal stress, $\sigma_n < 200$ MPa, he found

$$\tau = 0.85\sigma_n \quad (44)$$

and for higher normal stress

$$\tau = 50 + 0.6\sigma_n \quad (45)$$

τ is, again, the shear stress at failure and both stresses are measured in MPa. This friction law, referred to as *Byerlee's law*, is, with very few exceptions, independent of lithology. It holds over a very wide range of hardness and ductility (from carbonates to silicates) and is to first order independent of sliding velocity and roughness. Byerlee's law applies, in general, for temperatures below 400°C and can, due to its universality, be used to estimate the strength of natural faults.

Sliding on faults in the Earth's crust is often considered to take place on pre-existing planes of weakness where there is essentially no cohesion, i.e. $\tau_0 = 0$. Following *Jaeger and Cook* [1979] we can write the ratio of principal stresses for a crust in frictional equilibrium with one principal stress vertical as

$$\frac{\sigma_1}{\sigma_3} = \left(\sqrt{\mu_s^2 + 1} + \mu_s \right)^2 \quad (46)$$

where μ_s is the coefficient of sliding friction on pre-existing faults. This would give us the failure line **f2** in Figure 7, assuming that the sliding friction equals the internal friction.

If we study a crack that contains fluid at a pressure P , this pressure can be linearly superimposed on the applied stresses S_{ij} and we find that the effective stress σ_{ij} depends on the difference [*Scholz, 1990*]

$$\sigma_{ij} = S_{ij} - P\delta_{ij} \quad (47)$$

where δ_{ij} is the Kronecker delta. Most physical properties of porous solids change in response to changes in the effective stress, as opposed to changes in the applied stress. The effective stress law affects macroscopic strength as well, so the Coulomb criterion should be written as

$$\tau = \mu\sigma_n + \tau_0 = \mu(S_n - P) + \tau_0 \quad (48)$$

which agrees well with experiment [*Scholz, 1990*]. The pore fluid term will move the Mohr circles to the left, along the σ_1 axis or move the friction line to the right along the same axis, as **f3** in Figure 7A (**f3** additionally has $\tau_0 = 0$, this is just for ease of illustration in the figure).

3 Stress information from microearthquakes

Earthquake focal mechanisms are an excellent source of information on stress directions and relative stress magnitudes in the crust. In fact, as of 1997, 58% of the stress indicators in the World Stress Map database were from focal mechanisms [*Müller et al., 1997*]. In this section I will briefly introduce earthquake focal mechanisms and how to obtain estimates of the stress tensor from the mechanisms.

3.1 The seismic moment tensor

Since the work of *Reid* [1910] on the San Andreas fault before and after the 1906 San Francisco earthquake, it has been generally recognized that most earthquakes are caused by slippage on active geological faults. This process can be mathematically described either as a displacement discontinuity in the medium or in terms of body forces in an intact medium, which are applied to certain elements in the source region. The first approach can, however, be incorporated into the second by the use of body-force equivalents, i.e. outside the source region the seismic waves set up by slip on a fault are identical to the waves generated by a distribution of certain forces with canceling moments on the same fault [*Aki and Richards*, 1980]. Close to the source the force equivalents are non-unique, fault slip is equivalent either to two single-couples (a double-couple), Figure 8A, a single-couple plus a single-force system, Figure 8B, or a single-couple with any combination of single-couple to single-force system, all of which give no net force or net couple outside the fault region [*Aki and Richards*, 1980]. Far away from the source, where we usually only observe waves with wavelengths greater than the fault's linear dimension, the fault acts as a point source and the body-force equivalent to shear faulting is a double-couple. The strength of the couple, the *seismic moment* M_0 , is defined as $M_0 = \mu \bar{u} A$ where μ is the shear modulus and \bar{u} the average displacement over the active fault area A . In Figure 8A our hypothetical fault lies in the $x_3 = 0$ plane and slip occurs in the x_1 direction. In the point source approximation, where we only have one double-couple, the equivalent body-force description for a fault in the $x_1 = 0$ plane, with slip in the x_3 direction, is identical to the one above and we have the well known ambiguity between fault plane and auxiliary plane.

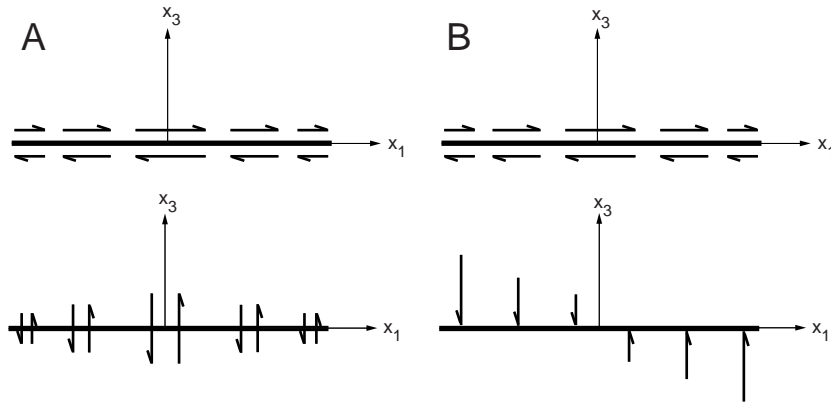


Figure 8: Distribution of body-forces equivalent to fault slip. The fault plane is the $x_3 = 0$ plane. A) Two single-couples (a double-couple). B) One single-couple and a system of single-forces. Modified after *Aki and Richards* [1980].

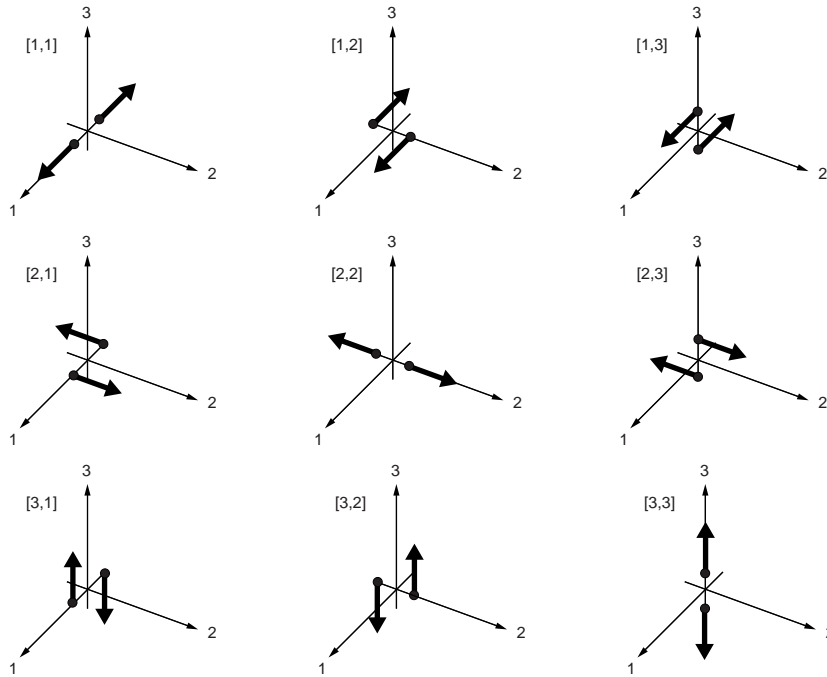


Figure 9: The nine generalized couples of the seismic moment tensor. Modified after *Aki and Richards* [1980].

There is no information in the radiation from an effective point source of slip that enables one to distinguish the fault plane from the auxiliary plane. If the double-couple description is generalized to arbitrary orientations in space and if we allow for discontinuities in displacements normal to the fault (this incorporates apparent expansions or compressions), there will be nine generalized couples forming the seismic *moment tensor* $\underline{\mathbf{M}}$, as shown in Figure 9. The tensor depends on the source strength and fault orientation and it characterizes all information about the source that can be obtained from observing waves with longer wavelength than the source dimensions [*Aki and Richards*, 1980]. The moment tensor is symmetric due to conservation of angular momentum, it is time dependent (following the temporal development of slip, see e.g. *Aki and Richards* [1980]) and can be written

$$M_{pq} = \mu A(\bar{u}_p \nu_q + \bar{u}_q \nu_p) \quad (49)$$

where \bar{u}_p is the average slip in the x_p direction on a plane with normal ν_q in the x_q direction and vice versa. The components of M_{pq} are, hence, the representations of forces in the x_p directions with moment arms in the x_q directions. In terms of the seismic moment and with the choice of coordinate axis made in Figure 8, the

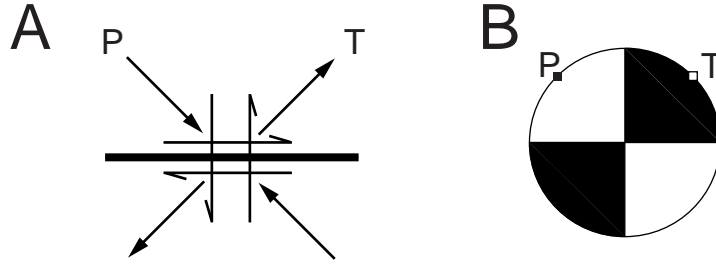


Figure 10: A) The double-couple force system and the equivalent force dipoles, the P and T axes. B) The “beach ball” representation of the double-couple mechanism in A. Quadrants where the first motion of the P-wave is compressional are black, the P and T axis directions are indicated with small squares.

moment tensor for the double-couple is

$$\begin{pmatrix} 0 & 0 & M_0 \\ 0 & 0 & 0 \\ M_0 & 0 & 0 \end{pmatrix} \quad (50)$$

As the moment tensor is real and symmetric, it can be rotated into a principal system where all off-diagonal elements are zero

$$\begin{pmatrix} 0 & 0 & 0 \\ 0 & -M_0 & 0 \\ 0 & 0 & M_0 \end{pmatrix} \quad (51)$$

This tensor shows the characteristics of a double-couple moment tensor; one eigenvalue is zero and the trace of the tensor is zero. We see that the double-couple is now represented by two force dipoles without shear, c.f. Figure 9, one compressive (the negative eigenvalue) and one tensile (the positive eigenvalue). The corresponding eigenvectors are $(0, 1, 0)$ for the null eigenvalue, also called the B axis, $1/\sqrt{2}(1, 0, -1)$ for the $-M_0$ eigenvalue, or the P (pressure) axis, and $1/\sqrt{2}(1, 0, 1)$ for the M_0 eigenvalue, or the T (tension) axis, see Figure 10. The P and T axes are always at 45° to the fault plane/auxiliary planes and always in the plane of the nodal plane normals, thus, in the plane of the double-couple force system.

The slipping fault is specified by three angles, see Figure 11. I use the convention established by *Aki and Richards* [1980], p. 106, for the angles of the strike, dip and rake of the fault plane solution. These angles can be used to parameterize the fault normal, \mathbf{n} , and slip, $\bar{\mathbf{u}}$, vectors, the moment tensor components M_{pq} and the P and T axes, i.e. the geometrical properties of a double-couple source is adequately described by the strike, dip and rake.

The seismic moment tensor is a convenient tool for calculating the displacement field from a seismic source, since once the Earth responses (the Green’s functions)

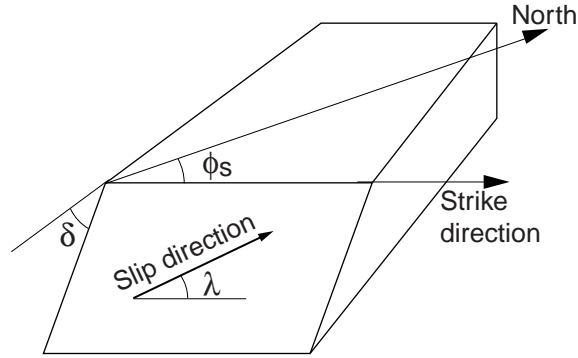


Figure 11: Definition of the angles used to describe a fault plane solution. ϕ_s is the azimuth of the fault strike with respect to North, $0 \leq \phi_s \leq 360$, δ is the dip of the fault plane from horizontal, $0 \leq \delta \leq 90$ and λ is the rake, or direction of slip, in the fault plane with respect to the horizontal, $-180 \leq \lambda \leq 180$. The rake is the direction of motion of the hanging wall with respect to the foot wall.

to the different moment tensor components have been computed, actual ground motion is just a linear combination of the responses weighted by the moment tensor components [Aki and Richards, 1980]. The moment tensor can accommodate other types of sources such as tensile faults, volume sources such as explosions or rapid phase transitions and also non-double-couple mechanisms, where there might be a net force, such as in landslides, volcanic eruptions or unsteady-fluid flow [Julian et al., 1998]

3.2 P and T axes and the stress tensor

As noted above, the P and T axes are force dipoles of an equivalent body-force description, generating seismic waves that have displacements indistinguishable from the displacements generated by a shear dislocation discontinuity. The diagonalized moment tensor for a double-couple source, with the P, B and T axes as principal axes, resembles a principal stress tensor with magnitudes $\sigma_1 = 1$ (or M_0), $\sigma_2 = 0$ and $\sigma_3 = -1$ (or $-M_0$). (Note that there is a sign difference in the definitions of the stresses, which are considered positive for compression, and the PT force dipoles, where tension is positive.) It is, however, important to distinguish between the crustal stress tensor and the P and T axes dipoles. McKenzie [1969] showed that only if the earthquake fractures homogeneous rock without internal friction is the P axis parallel to σ_1 . If, as is commonly observed, the earthquake occurs on pre-existing planes of weakness, the only restriction that can be placed on σ_1 is that it must be in the dilatational quadrant of the focal mechanism, i.e. within 90° of the P axis. Nevertheless, P and T axes are frequently used as approximations for the stress axes. If one assumes a coefficient of friction of $\mu = 0.6$

and if the fault plane is known, there is only a 15° difference in the orientation of the P axis and σ_1 . Great care has to be observed in these approximations, however. Consider earthquakes on the San Andreas fault (SAF) in California, USA. Large right-lateral strike-slip earthquakes on N-S striking subvertical faults are frequently observed on the SAF, yielding P axis directions of approximately $N45^\circ E$. The SAF is, however, known to be subjected to an almost fault normal direction of σ_1 [e.g. *Zoback and Beroza, 1993*], and the P axis approximation of σ_1 is 45° in error.

The direction of the maximum horizontal compressive dipole, P_H , is calculated in the same manner as the direction of maximum horizontal stress, σ_H , i.e. a vertical plane is inserted in the PT force dipoles and rotated until the horizontal compression is maximized [*Slunga et al., 1984*]. A mere projection of the P axis to the horizontal is not sufficient, especially when neither the P nor the T axis is close to horizontal or vertical. In the following I will refer to the horizontal compressive dipole as horizontal compression, or maximal horizontal compression, as computed from the PT dipoles. This is not to be confused with the horizontal stress, or maximum horizontal stress, which is calculated from the stress tensor.

As an illustration I compare P and T axes from two groups of events used in Paper IV with the stress tensors estimated for the two groups. Both groups consist of 40 events and were inverted for the causative stress tensor using the technique described in Paper II. Studying individual events I find, as expected, that a projection of the P axis to the horizontal only agrees with the proper maximum horizontal compression calculation when the P and T axes are either both subhorizontal or one subhorizontal and one subvertical. For example, for a P axis with trend 129.1° and plunge 39.8° and T axis with trend 358.7° and plunge 37.9° the direction of maximum horizontal compression is $N108.2^\circ E$, a 21° difference from the horizontal projection of the P axis. The first group of events yielded a rather well constrained stress tensor of oblique strike-slip with a normal faulting component, σ_1 trending 214° with plunge 30° , and σ_3 having trend 306° and plunge 4° . This gives a direction of σ_H of $N34.8^\circ E$. Calculating the average P_H axis for the group I obtain $N39.8^\circ E$, with a standard deviation of 10.1° and a range between $N1.4^\circ E$ and $N70.5^\circ E$, i.e. the average horizontal compression axis agrees quite well with the horizontal stress direction but individual earthquakes can have large deviations in their orientations. Stress inversion of the second group produced a normal faulting stress regime but with σ_1 and σ_2 having equal magnitudes, implying a strike-slip component. This stress estimate was less well constrained than that for group 1 and this is reflected in the average P, T and P_H axes directions, which have larger ranges. The direction of σ_H is $N64.4^\circ E$ and the average P_H direction $N62.7^\circ E$, with standard deviation 16.4° and range $N23.5^\circ E$ to $N122.0^\circ E$. I find that for a larger number of events the average of the P and the T axes are a reasonable approximation of the state of stress but that, in agreement with *McKenzie [1969]*, individual earthquakes cannot be used

to estimate the stress tensor with any confidence. The PT stress approximation also only yields directions and no information on the magnitudes of the stress components.

3.3 Determining fault orientations from seismic wave observations

There exists today a large number of inversion procedures for obtaining information about the seismic source. The simplest techniques use only P wave first motions to constrain the three angles of the fault plane solution. More advanced schemes use amplitudes or amplitude ratios to obtain the fault plane solution and a measure of the seismic moment M_0 . Even more complex inversions estimate the entire moment tensor with both double-couple and non-double-couple contributions. The stress tensor inversion technique described in paper II of this thesis and the spectral amplitude correlation scheme in paper III, were developed on the basis of the source mechanism inversion by *Slunga* [1981], later extended by *Rögnvaldsson and Slunga* [1993]. The techniques in paper II and III are not limited to a certain focal mechanism inversion technique, but their development was inspired by features of the *Slunga* [1981] technique, which is why I will point out the main ideas behind his approach, which I will refer to as the RS-technique.

Developed for use in local networks with source-receiver distances of less than 100 km, the RS-technique assumes a pure double-couple source without overshoot in the source-time function. Under such circumstances the P and S wave far-field impulses are only dependent on the fault plane solution and the seismic moment. Using the absolute values of the spectral amplitudes (the low-frequency asymptote) for P, SV and SH waves plus the first motion directions of the P wave, the RS-technique performs a grid search over strike, dip and rake, calculates the radiation pattern and, if the radiation pattern agrees with the polarity readings, performs a direct, least-squares inversion for the seismic moment. The misfits from the inversions are compared and an optimal, best-fitting focal mechanism is found. Of great importance for the stress tensor inversion in paper II is the fact that the RS-technique not only yields an optimal focal mechanism with associated errors, but also produces a range of well fitting, acceptable, focal mechanisms. These acceptable mechanisms have source orientations and slip directions that satisfy the recorded spectral amplitudes and polarities and give sufficiently small least-square misfits, which we will refer to as amplitude errors. The number of acceptable mechanisms obtained in the inversion depends on the shape of the objective function and usually varies between 10 and 90. Events with poorly restricted focal mechanisms have a larger number of acceptable mechanisms. This provides the stress inversion routine with a measure of the non-uniqueness of the focal mechanism and a range of mechanisms, that all fit the data, to test in the inversion scheme.

The RS-technique was successfully tested on Swedish earthquakes in the 1970s and 1980s and is incorporated into the routine analysis of the Icelandic seismic network SIL (Section 5.2). Focal mechanisms produced using the RS-technique have been compared to moment tensors produced using full waveform inversion [Shomali and Slunga, 2000]. Icelandic earthquakes of $M_L \sim 4$ were used and there was generally good agreement between the two approaches.

3.4 Inverting focal mechanisms for the stress tensor

We learned from the work of *McKenzie* [1969] that the crustal stress tensor cannot be estimated with confidence from the focal mechanism of one earthquake. Instead, we need an inversion mechanism that allows us to estimate the stress tensor from a larger number of earthquakes, and to formulate such a mechanism we will turn to structural geology and studies of faulting for help. The basic principles for slip on an arbitrarily oriented fault in a stress field were formulated by *Wallace* [1951] and *Bott* [1959]. *Bott* [1959] also proposed that slip on any fault plane will occur in the direction of maximum resolved shear stress (Bott's criterion) and showed, as in Equation 19, that the shear stress direction does depend on the orientation of the fault plane in the stress field and the relative size of the intermediate stress, R , but does not depend on the actual principal stress magnitudes. In his paper, *Bott* [1959] suggests that his equations could be used to determine the stress orientations and R , but it was not until *Carey and Brunier* [1974] utilized Bott's criterion that an inversion scheme for the causative state of stress was formulated. *Carey and Brunier* [1974] added the assumption that the motion shown by striae on the fault planes in their data set were all caused by a single common stress tensor. Their analysis was extended and improved on by a number of authors [e.g. *Angelier*, 1979; *Etchecopar et al.*, 1981; *Angelier et al.*, 1982; *Armijo et al.*, 1982; *Michael*, 1984; *Reches*, 1987; *Angelier*, 1990]. In common for most of these authors is the use of the geometric information of strike, dip and rake of the fault data for the estimation of the reduced stress tensor \underline{T} , i.e. the directions of the principal stresses and the ratio R . The reduced stress tensor is equivalent to finding four of the six independent components of the stress tensor. The last two, the magnitude of the maximum shear stress ($\sigma_1 - \sigma_3$) and an isotropic component, cannot be determined without additional information. Estimating four parameters imply that we need at least four earthquake focal mechanisms as input data, see however the data discussion in Section 3.4.1 below. Inverting the fault plane measurements without other constraints than the ones of stress homogeneity and Bott's criterion discussed above, is a highly non-linear process. The papers quoted above use a wide variety of numerical techniques for the stress inversion and some add constraints to linearize the problem in their methods. *Angelier* [1979] proposed both an iterative inversion minimizing the angle between the calculated maximum shear direction and the slip direction in the fault plane, and a direct least-squares (LS)

inversion minimizing the calculated shear stress perpendicular to the slip in the fault plane. The iterative LS-inversion scheme developed by *Angelier et al.* [1982] incorporates the errors of the fault plane measurements, *Michael* [1984] linearized the problem by requiring that the shear stress magnitudes on all failing faults are similar, *Reches* [1987] used the constraint that shear and normal stresses on the faults are related by a Coulomb failure criterion and *Angelier* [1990] minimized the angle between slip direction and shear stress while requiring large shear stress magnitudes to obtain a linearized inversion scheme. All these different approaches can yield a variety of results and, especially, very different error estimates.

Generalizing these inversion schemes from geological fault slip measurements to earthquake focal mechanisms [e.g. *Vasseur et al.*, 1983; *Gephart and Forsyth*, 1984; *Angelier*, 1984; *Michael*, 1987; *Carey-Gailhardis and Mercier*, 1987] is rather straightforward but introduces the problem of the two nodal planes. We know from the double-couple discussion in section 3.1 that there are two indistinguishable nodal planes for each focal mechanism. Which is the “correct” plane, which plane did slip in the earthquake, which plane should be used to infer the causative state of stress? Using focal mechanisms in a stress inversion scheme requires us to either choose one of the nodal planes or to justify incorporating both. *Angelier* [1984] experimented with the inclusion of both nodal planes, inferring axisymmetric stresses ($R = 0$ or 1) in which case both nodal planes are equally plausible. *Gephart* [1985] later showed that this is strictly admissible only if the B axis is coplanar with the two equal stress axes. Another common approach to the nodal plane problem is to choose the nodal plane which best fits surface geological evidence of fault orientations [e.g. *Angelier*, 1984; *Gephart*, 1990]. However, extrapolating surface fault orientations to earthquake focal depths is not always possible, an area can have complex surface faulting structures that are difficult to use to constrain the earthquake nodal planes. One might also wish to estimate subsurface fault structure using the stress inversion. In such cases the stress inversion technique itself must choose a preferred nodal plane. One method of picking the fault plane is to test both nodal planes in the stress field under consideration and choose the nodal plane which has the smallest angle between the shear stress and the slip direction (angular deviation) [e.g. *Vasseur et al.*, 1983; *Gephart and Forsyth*, 1984; *Bergerat et al.*, 1998]. I will refer to this method as the slip angle method. Tested by *Michael* [1987], the method works satisfactory when there are large differences in the angular deviations between the nodal planes. In more difficult situations, however, the reliability can become much degraded, see e.g. *Magee* [1997] and Paper II. *Carey-Gailhardis and Mercier* [1987] suggested an alternate fault picking mechanism; for each stress state they calculate an apparent value of R for each nodal plane and since for non-axisymmetric stresses only one of the nodal planes can have R in the allowed range $0 \leq R \leq 1$ [*Gephart*, 1985], the “good” nodal plane is picked. A method for choosing nodal plane based on a stability criterion is presented in Paper II of this thesis.

The grid search inversion method by *Gephart and Forsyth* [1984] introduced a novel approach to the angular deviation, or measure of misfit. Previously the misfit angle was usually defined as the angle between the tested shear stress direction and the observed slip direction in the fault plane. *Gephart and Forsyth* [1984] showed that this implicitly only considers errors in the slip direction but not in the orientation of the plane. They instead defined the misfit angle as the minimum rotation angle between the observed slip direction and the family of admissible fault geometries. *Gephart and Forsyth* [1984] also utilized a one-norm misfit criterion instead of an LS-criterion, based on observations that the angular misfit residuals were better fit by an exponential distribution than a normal distribution. *Carey-Gailhardis and Mercier* [1987] tested the fault planes obtained in the stress inversion against the first motion data from the focal mechanisms. This approach was used in conjunction with the *Gephart and Forsyth* [1984] inversion by *Magee* [1997] to better constrain the stress inversion and further utilizing the basic seismological data, *Horiuchi et al.* [1995] developed a completely integrated focal mechanism and stress tensor inversion based on polarities.

Paper II of this thesis introduces a stress tensor inversion technique based on the *Gephart and Forsyth* [1984] method but with considerable extensions in terms of allowing for the misfit of the earthquake focal mechanisms and in the choice of nodal plane.

3.4.1 On the distribution of data

Many of the authors referred to above have pointed out that the distribution of data is important for the success of the stress tensor inversion schemes. We noted above that we need at least four earthquake focal mechanisms to constrain the four parameters in the inversion. In addition, the focal mechanisms have to be sufficiently well distributed in terms of nodal plane orientations. A large number of earthquakes on similarly oriented faults with similar slip directions will not constrain the stress tensor more than one or two events having those orientations. (Many events on similarly oriented faults with significantly varying slip is, obviously, an indication of heterogeneous stress or bad data.) It is hence important to assess the information available in, or the redundancy of, the input data in terms of sufficiently well distributed focal mechanisms. An additional problem with redundant data is the calculation of the confidence limits. Using the total number of events in the calculation often under-estimates the size of the confidence regions due to data redundancy. *Magee* [1997] addressed the problem by assigning both nodal plane normals for all events to 10° bins over the lower hemisphere. She then used half of the number of filled bins as the number of non-redundant events to use for the confidence limits calculations. This limited the possible number of non-redundant events to 101.

In Paper III we present a different solution to the problem of redundant data through an assessment of the events' focal mechanisms based on spectral amplitude data.

3.4.2 Magnitudes of the principal stresses

In order to calculate stress magnitudes for the directions and R value obtained from stress inversion of earthquake focal mechanisms we need to introduce additional information on the stress tensor. This is usually done by using a failure criterion to constrain the $\sigma_1 - \sigma_3$ magnitude and by normalizing the vertical stress to one. Absolute magnitudes of the principal stresses can then be obtained by assuming that the vertical stress equals the weight of the overburden. I utilize the Coulomb failure criterion, see Equation 48, to obtain the principal stress magnitudes. Rewriting the Coulomb criterion in terms of the principal stresses, the necessary equations can be written

$$\sigma_1 = \sigma_3 \left(\sqrt{\mu^2 + 1} + \mu \right)^2 + C_0 \quad (52)$$

$$R = \frac{\sigma_1 - \sigma_2}{\sigma_1 - \sigma_3} \quad (53)$$

$$S_V = S_1 \sigma_{1d}^2 + S_2 \sigma_{2d}^2 + S_3 \sigma_{3d}^2 \quad (54)$$

R is the stress ratio introduced above, S_V the vertical stress and the $S_i \sigma_{id}$ are the vertical components of the principal stresses. Setting $\mathcal{M} = (\sqrt{\mu^2 + 1} + \mu)^2$ and normalizing with the vertical stress, S_V , so that $\sigma_i/S_V = (S_i - P)/S_V = s_i - p_0$, where s_i are the normalized principal stress magnitudes, and $c_0 = C_0/S_V$ the normalized compressive strength, we find from Equation 52

$$s_1 = s_3 \mathcal{M} + p_0(1 - \mathcal{M}) + c_0 \quad (55)$$

and from Equation 53

$$s_2 = s_1(1 - R) + s_3 R \quad (56)$$

Setting $\mathcal{X} = p_0(1 - \mathcal{M}) + c_0$ and substituting Equations 55 and 56 in Equation 54 we obtain the final equations for the normalized stress magnitudes.

$$s_3 = \frac{1 - \mathcal{X}(\sigma_{1d}^2 + (1 - R)\sigma_{2d}^2)}{\mathcal{M}\sigma_{1d}^2 + (\mathcal{M}(1 - R) + R)\sigma_{2d}^2 + \sigma_{3d}^2} \quad (57)$$

$$s_2 = s_3(\mathcal{M}(1 - R) + R) + \mathcal{X}(1 - R) \quad (58)$$

$$s_1 = s_3 \mathcal{M} + \mathcal{X} \quad (59)$$

It can sometimes be valuable to express the crack fluid pressure, or pore pressure, as a fraction of σ_3 and if the derivation above is repeated with $p_x = P/S_3$ and $\mathcal{Y} = \mathcal{M}(1 - p_x) + p_x$, we find for the normalized stress magnitudes

$$s_3 = \frac{1 - c_0(\sigma_{1d}^2 + (1 - R)\sigma_{2d}^2)}{\mathcal{Y}\sigma_{1d}^2 + (\mathcal{Y}(1 - R) + R)\sigma_{2d}^2 + \sigma_{3d}^2} \quad (60)$$

$$s_2 = s_3(\mathcal{Y}(1 - R) + R) + c_0(1 - R) \quad (61)$$

$$s_1 = s_3 \mathcal{Y} + c_0 \quad (62)$$

The stress magnitudes can then be calculated using appropriate values for the coefficient of friction, μ , the pore pressure P and the uniaxial compressive strength of the rock C_0 .

4 Stress information from deep boreholes

As alluded to in the Introduction, the need to measure *in situ* stresses in civil, mining and petroleum engineering, as well as in geology and geophysics, has led to the development of a large number of stress measurement techniques. In this section I will only discuss a few of these techniques, concentrating on the methods used in stress measurements in deep boreholes. For a comprehensive review of current rock stress measurement techniques the interested reader is referred to *Amadei and Stephansson* [1997].

While the methodology for determining the orientation and relative magnitude of *in situ* stresses is now well-established [e.g. *Zoback and Zoback*, 1980, 1989, 1991] and has been utilized at literally thousands of sites around the world [e.g. *Zoback*, 1992], there have been extremely few sites where *in situ* stress magnitude has been measured at depths greater than 2-3 km, see review in *Brudy et al.* [1997]. This is in part due to the very few deep boreholes drilled but also because conventional stress magnitude measurement techniques, e.g. overcoring and hydraulic fracturing, are technically extremely difficult in deep boreholes. Recent developments [*Brudy and Zoback*, 1993; *Peška and Zoback*, 1995; *Brudy and Zoback*, 1999] in the interpretation and analysis of drilling-induced compressive and tensile failures in wellbore image data have, however, made stress orientation and magnitude estimation considerably easier and also allow for a continuous stress profile along the borehole. The use of an “integrated stress measurement strategy” (ISMS) for continuous stress orientation and magnitude estimation was first reported from the Cajon Pass borehole [*Zoback and Healy*, 1992] and was further extended [*Brudy et al.*, 1997] in the stress analysis of the KTB deep borehole. The ISMS involved a combination of direct measurement of the least principal stress, using hydraulic fracturing, and detailed analysis of extensive drilling-induced wellbore failure. For later reference I have included, see Figure 12, the stress profiles from the Cajon Pass borehole [*Vernik and Zoback*, 1992] and from the KTB main borehole [*Brudy et al.*, 1997]. An ISMS is utilized in Paper I of this thesis and I will briefly review the new wellbore image data methods here, starting however with the well-established but very important hydraulic fracturing method.

4.1 Hydraulic fracturing

Determination of the state of stress in boreholes using the hydraulic fracturing method is common today and can be utilized to a considerable depth and in almost any rock formation. The hydraulic fracturing method assumes that the borehole

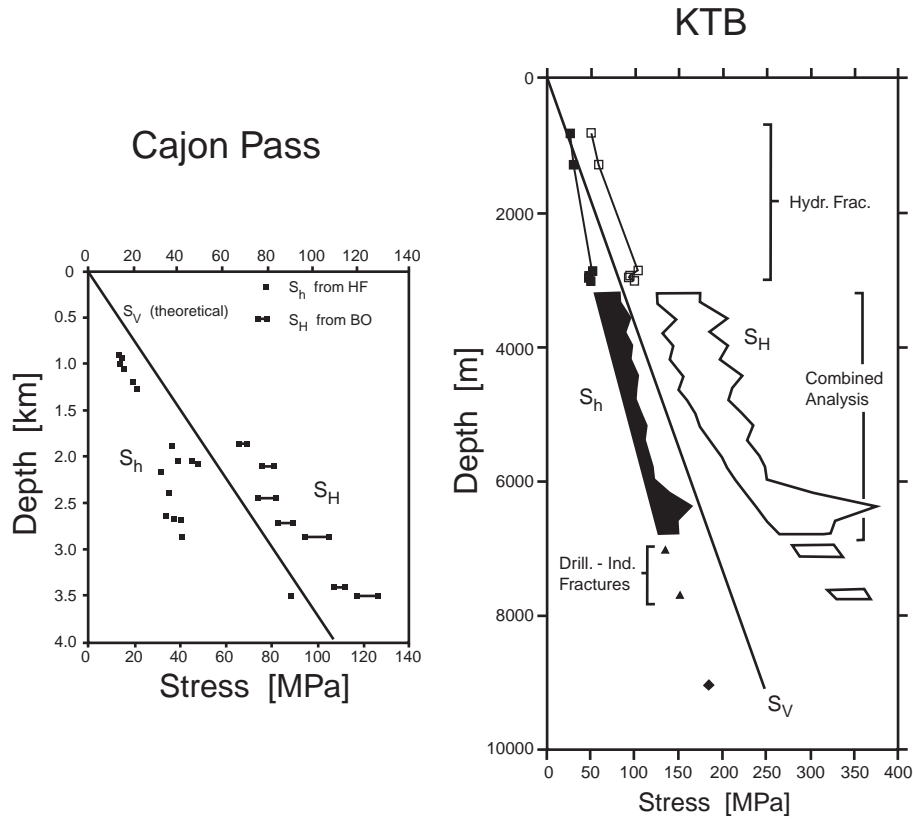


Figure 12: State of stress inferred from the Cajon Pass and KTB scientific boreholes, both drilled into crystalline rock. Left) Stress profile from the Cajon Pass borehole using the hydrofracturing data of *Zoback and Healy* [1992] for S_h and the borehole breakout analysis of *Vernik and Zoback* [1992] for S_H , assuming nonporous rock ($\alpha = 0$). Figure modified from *Vernik and Zoback* [1992]. Right) Stress profile from the KTB boreholes. Stress magnitudes from hydraulic fracturing in the pilot hole is shown as solid, S_h , and open, S_H , squares. Between 3 km and 6.8 km, the results from the combined analysis of borehole breakouts and induced tensile fractures have been merged into a solid, S_h , and an open, S_H , polygon. Below 6.8 km the S_H magnitude is only calculated from tensile fractures. At 7, 7.7 and 9 km km only the estimation for the least possible S_h magnitude is shown. Figure modified from *Brudy et al.* [1997].

is drilled parallel to a principal stress direction, which is usually considered valid for vertical boreholes, see Section 2.1. It is also important to have a test interval free of natural fractures, since these would render the results invalid (*Cornet and Valette* [1984] introduced a hydraulic test on pre-existing fractures, the HTPF method). In a hydraulic fracturing test a section of the borehole is sealed off by

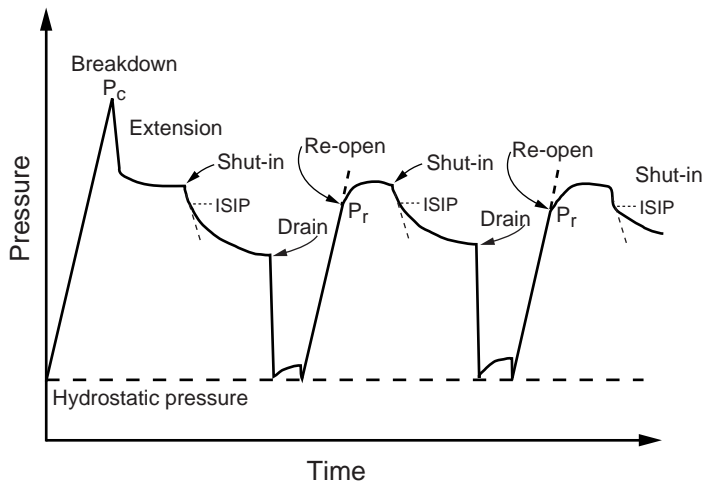


Figure 13: Pressure-time curve of a typical hydraulic fracturing experiment showing three pressurization cycles. The first cycle achieves a breakdown of the formation, whereas the two following cycles reopen the newly created fracture. During the shut-in phase the shut-in pressure, ISIP, is observed, which is identical to the least principal stress. Modified after *Brudy* [1995].

packers, to prevent borehole fluid from escaping up or down the borehole. Fluid is pumped into the sealed-off section and with increasing fluid pressure the hoop stress, $\sigma_{\theta\theta}$, at some points on the borehole wall will become tensile and when the tensile strength of the rock is exceeded a fracture will form in the borehole wall. The fracture will propagate perpendicular to the least principal *in situ* stress, σ_3 . Figure 13 shows a typical pressure versus time curve.

The injection interval is pressurized very rapidly in the beginning of the first cycle, causing a linear pressure increase with time. This is in order to attain the breakdown pressure, P_c , as quickly as possible, avoiding that the borehole fluids invade the host rock. Penetration of borehole fluids will cause the pore pressure in the host rock to increase, thus decreasing the effective stress and triggering a premature breakdown of the formation. At the breakdown pressure, a fracture initiates in the borehole wall where the hoop stress is most tensile ($\theta = 0$ in Equation 26), exceeding the tensile strength of the host rock, i.e. $\sigma_{\theta\theta} \geq -T$. Although well-established and frequently used, there is still some discussion as to which formulation should be used for the calculation of the maximum horizontal stress using the breakdown pressure. For a borehole in porous rock with non-penetrating borehole fluid, the breakdown pressure is

$$P_c = 3S_h - S_H - P_0 + T \quad (63)$$

as derived by *Hubbert and Willis* [1957], where P_0 is the formation pore pressure

and T is the tensile strength. If the borehole fluid penetrates the formation, the breakdown pressure equation is modified

$$P_c = \frac{3S_h - S_H - 2\eta P_0 + T}{2(1 - \eta)} \quad (64)$$

where η is the poroelastic coefficient

$$\eta = \frac{\alpha(1 - 2\nu)}{2(1 - \nu)} \quad (65)$$

with ν being Poisson's ratio of the formation and $\alpha = 1 - K/K_s$ the Biot coefficient, K and K_s are the bulk moduli of the rock constituents (grains) and the rock bulk, respectively. Equation 64 is part of the analysis of hydraulic fracturing presented by *Haimson and Fairhurst* [1967, 1970]. A third approach was suggested by *Schmitt and Zoback* [1989] using an effective stress law of the type

$$\sigma_{ij} = S_{ij} - \beta P_0 \delta_{ij} \quad (66)$$

where β is a constant between 0 and 1 that depends on the porosity. This will replace the equations above with

$$P_c = 3S_h - S_H - \beta P_0 + T \quad (67)$$

for a non-penetrating fluid and

$$P_c = \frac{3S_h - S_H - 2\eta P_0 + T}{1 + \beta - 2\eta} \quad (68)$$

for fluid penetration. The introduction of the effective stress law lends support to the elimination of the pore pressure term when interpreting hydrofracturing data from low permeability, hard granitic rocks [e.g. *Bjarnason et al.*, 1989; *Vernik and Zoback*, 1992; *Brudy and Zoback*, 1999].

Further pumping into the injection interval leads to propagation of the newly created fracture into the formation. Pumping is then stopped and the interval is shut-in. Borehole fluid will continue to flow into the growing fracture from the test interval and the fluid will also infiltrate into the fracture walls, causing the rapid decrease in pressure observed in the early shut-in phase. Once the asperities on the fracture walls make contact the pressure drop rate will decrease substantially and create a corner in the pressure-time curve, see Figure 13. The shut-in pressure, ISIP in Figure 13, is estimated from this corner, marking the lowest pressure for which the borehole fluid carries the complete load of the stress perpendicular to the fracture. Since the fracture is created perpendicular to σ_3 , the shut-in pressure equals the σ_3 magnitude. The pressure is then released, allowing the injection interval, the fracture and the host rock to drain back to hydrostatic pressure.

The pressurization cycle is repeated, commonly three or four times. Again, the pressure increase is first rapid and linear but then becomes non-linear. The point

of deviation from non-linearity marks the reopening pressure, P_r , of the fracture, and is lower than P_c due to the now negligible tensile strength

$$P_r = 3S_h - S_H - \beta P_0 \quad (69)$$

using the *Schmitt and Zoback* [1989] formulation. Additional pumping will open the fracture further and drive more fluid into the formation. Another shut-in phase follows, then drainage and repressurization. There are various methods to accurately determine P_c , P_r and the shut-in pressure.

Bredehoeft et al. [1976] suggested that the tensile strength of the formation could be determined from the difference between the breakdown pressure and the reopening pressure, assuming that the fracture closes completely between cycles. This implies determining the maximum horizontal stress as

$$S_H = 3S_h - P_r - \beta P_0 \quad (70)$$

The orientation of the hydraulic fracture, and thus the orientation of σ_H , is determined either by an impression packer or by borehole televiewer or Formation MicroScanner logging of the test interval.

Performing hydraulic fracturing tests in very deep boreholes is very difficult [e.g. *Gustafsson and Rhén*, 1990; *Brudy et al.*, 1997]. Pressures and flow rates have to be high, which is technically demanding for the equipment. Due to difficulties in reaching the breakdown pressure, pressure-time records can be troublesome to interpret. Both in the Gravberg-1 borehole, in Siljan, Sweden, and in KTB, the deeper hydraulic fracturing tests could only give a lower bound on σ_3 , see Paper I and *Brudy et al.* [1997], respectively.

4.2 Borehole breakouts

Breakouts are zones of failure of the borehole wall which form symmetrically at the azimuth of the least principal horizontal stress [e.g. *Bell and Gough*, 1979; *Zoback et al.*, 1985, and many others], see Figure 14. The breakouts are frequently elongated in the direction of the borehole axis, and can be described by three parameters; orientation in the borehole θ_b , opening angle $2\phi_b$ and radial depth r_b , see Figure 14. There are currently two mechanisms thought to be responsible for the formation of breakouts, both due to the stress concentration around the borehole (see Section 2.3). *Gough and Bell* [1982] and *Zoback et al.* [1985], followed by refined analysis by other authors, suggest that if the difference in horizontal magnitude between the two horizontal principal stresses is sufficiently large, breakouts will form in compressive shear failure. The opening angle can be empirically related to the far-field principal stresses [*Barton et al.*, 1988; *Vernik and Zoback*, 1992; *Haimson and Song*, 1993], and if the breakout shape is described as the area where the rock stresses overcome the *in situ* compressive strength, C_{eff} , the onset

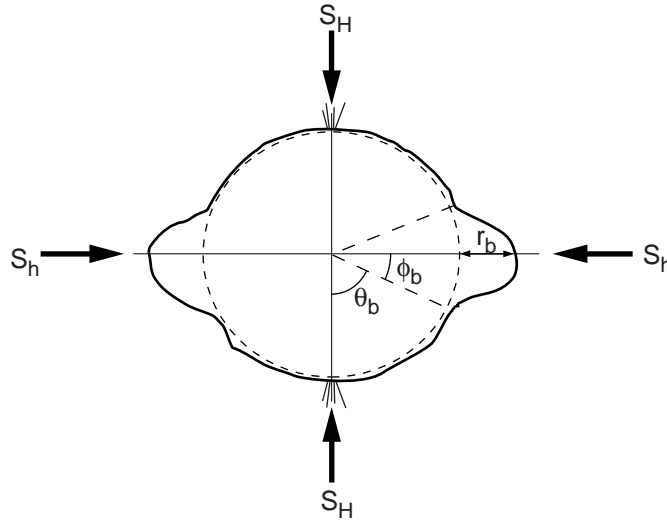


Figure 14: Borehole breakout in the wall of a vertical borehole subject to the maximum, S_H , and minimum, S_h , principal horizontal stresses. θ_b is the breakout orientation, ϕ_b the breakout opening half-angle and r_b the breakout depth.

of breakouts can be formulated as

$$\sigma_{\theta\theta}(\theta_b) = S_H + S_h - 2(S_H - S_h) \cos 2\theta_b - \Delta P = C_{eff} \quad (71)$$

where θ_b is the angle from the maximum horizontal stress S_H to the onset of the breakout, see Figure 14, and ΔP is, again, the difference between the borehole fluid pressure and the pore pressure in the host rock. The relation between the breakout onset angle θ_b and the breakout opening angle ϕ_b is

$$\theta_b = \pi/2 - \phi_b \quad (72)$$

Assuming that the effective rock strength C_{eff} can be properly estimated, Equation 71 can be used to estimate the magnitude of S_H . For the second breakout formation mechanism, *Zheng et al.* [1989]; *Lee and Haimson* [1993] and others propose that there is tensile splitting involved in the formation of breakouts. *Brudy et al.* [1997] reports from the KTB borehole that both mechanisms can be identified in rock samples and cuttings: compressive shear failure and extensional splitting of flakes due to the high tangential stress and a lack of “confining pressure” from the drill fluid. How breakouts stabilize is a subject still undergoing debate, see e.g. *Zheng et al.* [1989]; *Cheatham* [1993].

A variety of logging tools have been utilized to analyze borehole breakouts. 4-arm caliper, or dipmeter, logs can be used with appropriate caution not to interpret zones of complete wellbore failure or zones eroded by the drill-string (key seats)

as breakouts. See *Plumb and Hickman* [1985] or Paper I for a description of caliper data analysis. The resolution of caliper data is, however, low and there is no information on the width of the breakouts, i.e. the breakout orientation angle θ_b is 90° . Formation MicroScanner (FMS) [*Ekstrom et al.*, 1987], or Formation MicroImager (FMI), logging instruments measure microresistivity profiles in the borehole wall and give much higher resolution and better coverage of the borehole wall. These instruments do require four pads to follow the wellbore, which can be difficult if the breakouts are large, as in the Gravberg-1 borehole, see Paper I. The best coverage of the borehole wall is obtained by a borehole televiewer (BHTV) instrument [*Zemanek et al.*, 1970]. The BHTV emits acoustic pulses while rotating around the axis of the borehole. Travel time and amplitude of the reflected signals are measured and the travel-times converted to radial distance. This gives, under appropriate borehole fluid conditions, an excellent view of the borehole wall. All three parameters describing the breakouts can be measured from the logs, and comparisons made by e.g. *Shamir and Zoback* [1992] shows that the BHTV logs are superior to caliper logs for breakout analysis. All the above logging tools allow a continuous assessment of stress orientations in the borehole, the BHTV (and in some cases FMS/FMI) technique also allows a continuous assessment of S_H magnitude if the magnitude of S_h is known, e.g. from hydraulic fracturing measurements.

In spite of the still not fully resolved issues of formation and stabilization, it has been found that borehole breakouts in vertical boreholes can reliably be used as indicators of the direction of the least horizontal principal stress [e.g. *Zoback et al.*, 1985; *Plumb and Hickman*, 1985; *Dart and Zoback*, 1985], and breakouts have been utilized in numerous studies all over the world to assess stress orientation [*Zoback*, 1992].

In deviated boreholes, breakouts cannot be used directly to assess stress directions [*Mastin*, 1988] since the point of most compressive stress concentration around the wellbore is affected by the orientation of the borehole and the magnitudes of all three principal stresses. *Qian and Pedersen* [1991] utilized this in a non-linear inversion scheme and the situation was analyzed in detail by *Peška and Zoback* [1995] who showed that under appropriate circumstances it is possible to use breakouts in deviated boreholes to assess both stress orientation and magnitudes.

The estimation of S_H using borehole breakouts is still a debated issue, see e.g. *Amadei and Stephansson* [1997]. The geometry of breakouts is controlled by the rock strength, as discussed above, but also by lithology, pre-existing fractures, drilling intensity and method, and hole diameter. Nevertheless, *Vernik and Zoback* [1992] used Equation 71, with care taken to avoid misinterpretations due to lithology and other factors, to estimate S_H in the Cajon Pass borehole. They used triaxial stress measurements on core samples and the effective strain energy failure criterion (ESEF) [*Wiebols and Cook*, 1968], which can be used to estimate rock

strength from polyaxial stress states, for the estimation of S_H . The S_H magnitudes were compared to the estimates of S_H from hydraulic fracturing [Zoback and Healy, 1992] and were found to be generally consistent. A similar approach was followed by Brudy *et al.* [1997] in the KTB borehole where S_H magnitudes were estimated from borehole breakouts and compared to hydraulic fracturing results where these were available. Estimating S_H from breakouts, a proper effective rock strength and S_h estimates from i.e. hydraulic fracturing, is a promising technique to assess the S_H magnitude also in very deep boreholes, as shown by Brudy *et al.* [1997] in KTB.

4.3 Drilling-induced tensile wall-fractures

The drilling process can induce not only borehole breakouts, as described above, but also small-scale tensile fractures in the borehole wall. This type of fractures have been reported from the KTB boreholes [Brudy and Zoback, 1993; Brudy *et al.*, 1997; Brudy and Zoback, 1999] and from the Soultz-sous-Forêts GPK1 borehole [Tenzer *et al.*, 1994; Nagel, 1994]. When analyzing borehole image logs (FMS/FMI and BHTV logs) for faults and fractures, not only sinusoidal traces (all around the borehole, indicating planar faults or foliation planes) were found but also pairs of traces parallel to the borehole axis but offset 180° were encountered. In addition, in some intervals there were fracture traces inclined to the borehole axis, offset 180° but not connected around the borehole [Brudy and Zoback, 1999]. Both these types of fracture traces offset 180° have been interpreted to be drilling-induced tensile fractures [Brudy *et al.*, 1997; Brudy and Zoback, 1999]. Evidence for this comes mainly from the KTB pilot and main boreholes. In the sections of the KTB pilot well that were cored and where logging indicated vertical fractures, no fractures were seen in the core. In contrast, natural fractures cross-cutting the borehole could always be correlated between logs and core. Neither in the pilot hole nor in the main borehole were there any indications of lost circulation or drilling fluids at the depths where these fractures were observed. Finally, the relative abundance of these fractures in the boreholes and the unlikeliness of drilling into natural fractures parallel to the wellbore axis would imply a very large population of pre-existing, near vertical, fractures. This seems unlikely since no such fractures were seen in almost 4 km of continuous core from the KTB pilot hole [Brudy and Zoback, 1999].

The initiation of drilling-induced tensile fractures can be described by the Kirsch [1898] equations, see Equations 25, and have been discussed by e.g. Moos and Zoback [1990] and Brudy and Zoback [1999]. In a vertical borehole, where one of the principal stresses is vertical, the induced tensile fractures form vertically along the borehole axis in the direction of the maximum horizontal stress, and the formation of the fractures follow the same equations as those describing hydraulic

fracturing, i.e. at the borehole wall

$$\sigma_{\theta\theta} = 3S_h - S_H - 2P_0 - \Delta P \leq T \quad (73)$$

where P_0 is the pore pressure in the formation and ΔP is the difference between the borehole fluid pressure P_b and P_0 . In addition to the tectonic stresses there are several factors induced by the drilling process that affects the stress around the wellbore. The drill fluid pressure varies with the composition of the fluid, with the pumping pressure maintained to circulate the drill fluid and is somewhat increased when running in the drill pipe. Thermal cooling of the wellbore by the drill fluid is another contributor to the stresses. When the cold (surface temperature) drill fluid is pumped down the borehole it is slowly heated but does not reach the undisturbed formation temperature and, hence, induce a radially varying temperature field that also depend on the thermal diffusivity of the rock and the radius of the borehole. For fracture initiation, only the stress at the borehole wall is considered and the thermal stress can then be calculated by the simple expression, [e.g. *Brudy and Zoback, 1993*]

$$\sigma_{Therm} = -\frac{\alpha E \Delta T}{1 - \nu} \quad (74)$$

where E is Young's modulus, ΔT the temperature difference between the undisturbed formation temperature and the temperature after circulating the drill fluid, ν is Poisson's ratio and α the thermal expansion coefficient. The thermal expansion coefficient is best represented as the average of the thermal expansion coefficients of the mineral constituents. This is investigated in some detail in Paper I. The elastic parameters E and ν can be determined either through laboratory analysis of the core or derived using sonic logs from the borehole [*Brudy and Zoback, 1999*].

In order to use the drilling-induced fractures to estimate the magnitude of S_H we need to determine the tensile strength. In hydraulic fracturing this is important since the fracture is created in sections of the borehole where no pre-existing, natural fractures exist. The drilling-induced fractures, in contrast, have been observed in sections containing natural fractures [*Brudy and Zoback, 1999*] and Paper I, and are thought to initiate on small flaws in the borehole wall where no tensile strength has to be overcome. The tensile strength is, thus, neglected in the analysis [*Brudy et al., 1997; Brudy and Zoback, 1999*] and we have

$$S_H = 3S_h + \sigma_{Therm} - 2P_0 - \Delta P \quad (75)$$

for fracture initiation. We see that the magnitude of the least horizontal principal stress has to be determined before the magnitude of S_H can be calculated. This is normally done by a number of hydraulic fracturing tests that measures S_h and then S_h values are interpolated in the intervals between the measurements. In near-vertical boreholes, drilling-induced tensile fractures have been observed to form almost exclusively in strike-slip regimes where there is appreciable difference

in the magnitudes of the maximum and minimum horizontal stresses [Moos and Zoback, 1990; Peška and Zoback, 1995]. The drilling-induced tensile fractures do not propagate away from the borehole wall due to the rapid increase in compressive stress with distance from the wellbore [Brudy and Zoback, 1999].

In a deviated borehole the formation of drilling-induced tensile fractures depend on the orientation and magnitude of all three principal stresses, this situation has been analyzed in detail by Peška and Zoback [1995].

In conclusion, drilling-induced tensile wall fractures are promising as a means to assess both the orientations and magnitudes of the principal stresses in boreholes where conventional hydraulic fracturing is difficult. The method also provides a continuous stress profile along the borehole which would be very costly using hydraulic fracturing, even in shallow boreholes.

5 Iceland and the SIL network

All of the earthquake related research described in this thesis has been performed on microearthquakes recorded by the Icelandic SIL network. In order to set the stage for Papers II to IV, I will give a very brief introduction to the tectonics of Iceland and a short description of the operation of the SIL network.

5.1 Brief introduction to the tectonics of Iceland

Iceland is situated across the Mid-Atlantic ridge on top of a mantle plume, Figure 15. The center of the mantle plume is inferred to be beneath the east-central part of Iceland [e.g. Tryggvason *et al.*, 1983; Allen *et al.*, 1999] and due to the westward drift of the plate boundary with respect to the hotspot, the spreading zones successively jump eastward [Einarsson, 1991]. The divergent plate boundary in Iceland is thus offset to the east compared to the Mid-Atlantic ridge offshore to the north and south. From the south, see Figure 15, the Mid-Atlantic Ridge connects to the Reykjanes peninsula and continues onshore to the Hengill triple junction, where the spreading zone continues north along the Western Rift Zone (WRZ). East from the triple junction is a transform zone, the South Iceland Seismic Zone (SISZ), which connects the WRZ with the Eastern Rift Zone (ERZ). The ERZ extends northward to the Vatnajökull glacier and when the rift zone emanates from under the glacier in the north it is named the Northern Rift Zone (NRZ) and extends to the coast in the north. The Tjörnes fracture zone again connects the plate boundary to the Mid-Atlantic ridge. The spreading rate across Iceland is predicted by global plate motions, averaged over the last few million years, in the NUVEL-1A model [DeMets *et al.*, 1994] to approximately 19 mm/yr in the direction N76°W. The observed relative velocity of the North American plate (west of the WRZ) and the Eurasian plate (at the southern tip of the ERZ) is 21 ± 4 mm/yr in the direction N63°W $\pm 11^\circ$ [Sigmundsson *et al.*, 1995]. The

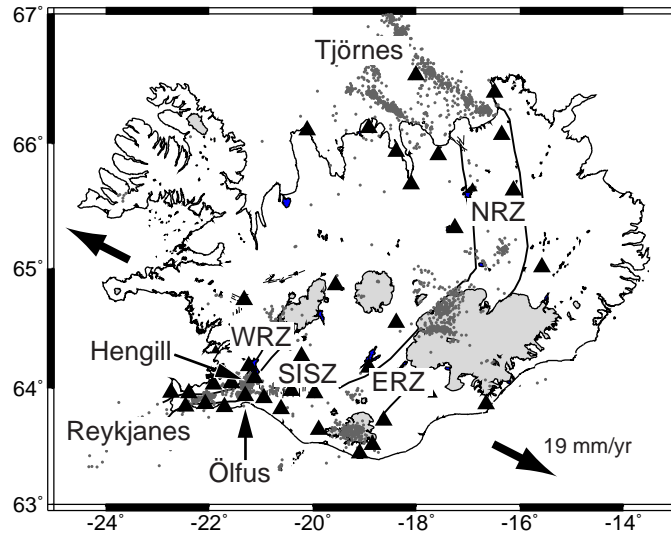


Figure 15: Map showing the rift and transform zones in Iceland. WRZ is the Western Rift Zone, SISZ, the South Iceland Seismic Zone, ERZ the Eastern Rift Zone and NRZ the Northern Rift Zone. The rate and direction of spreading is from *Sigmundsson et al.* [1995]. SIL seismic stations are shown as solid triangles. Small dots are earthquakes above magnitude 2.

Global Positioning System (GPS) measurements of *Sigmundsson et al.* [1995] indicate that about $85 \pm 15\%$ of the relative plate motion is accommodated by the SISZ in a 20 km to 30 km wide band that correlates well with the seismic activity in the SISZ.

The South Iceland Seismic Zone takes up the transform motion between the Reykjanes peninsula and the ERZ. There is, however, no large, east-west oriented transform fault in the SISZ, instead the transform motion is accommodated on many parallel, north-south right-lateral faults. The SISZ has seen a number of major earthquake sequences and large localized events such as the 1912 magnitude 7 earthquake west of Hekla [*Einarsson, 1991*]. Most of the large events are inferred to have occurred on N–S striking faults and much of the seismicity in the SISZ have strike-slip focal mechanisms [*Einarsson, 1991; Stefánsson et al., 1993*]. Surface mapping in the SISZ reveals a multitude of NNE and ENE striking faults, many with a strike-slip component, and NE striking normal faults [*Guðmundsson, 1995; Passerini et al., 1997; Bergerat et al., 1998*].

The Ölfus area is situated immediately south of the Hengill triple junction, in a transition region between the Reykjanes peninsula and the SISZ. In Reykjanes, earthquakes are mostly normal faulting, characterized by σ_3 being consistently horizontal, trending NW, and σ_1 rotating between vertical and horizontal, trending

NE [Einarsson, 1991]. Earthquakes in the Ölfus region are predominantly strike-slip, on N–S striking subvertical faults [Rögnvaldsson *et al.*, 1998] and surface fault and fissure mapping in the Ölfus region show that most faults strike N–S to NE–SW [Sæmundsson, 1995]. The Ölfus area will be discussed further in Papers II to IV.

5.2 SIL: The Icelandic seismic network

The South Iceland Lowland (SIL) project started in 1988 as a concerted effort of the Nordic countries towards earthquake prediction research in the South Iceland Seismic Zone [Stefánsson *et al.*, 1993]. The name SIL has since come to signify the initial project, the seismic network that was constructed during the project and the acquisition and analysis system developed for the network. The SIL network currently consists of 38 stations, concentrated mainly in the SISZ and the Tjörnes fracture zone, see Figure 15.

The description of the SIL network below is based on Böðvarsson *et al.* [1996] and Böðvarsson *et al.* [1999]. During the design phase of the SIL network, the importance of microearthquakes in earthquake prediction research and their significance for understanding the physical processes leading to earthquakes were generally recognized. This view emanated from the results from Californian dense networks and the results of monitoring and automatic processing in networks in Sweden. Retrieval of earthquakes down to magnitude $M_L = 0$ and source information for these events implied a new seismic network design. The SIL system is highly automatic and uses intelligent site stations to minimize data transmission costs.

Each station is equipped with a three-component seismometer (varying from 1 Hz Lennartz to broadband Guralp 3ESP), digitizer (16- or 24-bit), a GPS synchronized clock and a PC running the UNIX operating system. The SIL system uses single-station phase detections and multi-station event selection. Each detected transient is analyzed and the result is sent to the data center in Reykjavik in a 128 byte phase log structure via an X.25 link. Phase logs include onset time, duration, phase type (P or S), maximum amplitude, signal and noise averages, spectral parameters such as DC-level and corner frequency etc. Artificial neural networks are used to discern between P and S phases, increasing the correct identification of phases to over 95%. The stations are also equipped with software for continuous monitoring of ground velocity. The signals are bandpass filtered in three bands, 0.5 - 1 Hz, 1 - 2 Hz and 2 - 4 Hz, and an average amplitude value is computed every minute and sent to the center. Plots of these data give useful visual indication of seismic activity and have been used to monitor tremors accompanying volcanic activity and catastrophic floods from subglacial cauldrons.

At the center, the phases from the stations are associated and using iterative location, phase truncation, amplitude consistency and negative evidence (stations

without detections) events are defined. Only when an event has been defined does the system retrieve waveform data from the stations. Neural networks are under evaluation to aid in the complex phase association procedure. The routine analysis performed on every recorded earthquake includes estimation of the focal mechanism. The algorithm used by the SIL system was described in Section 3.3.

Multi-event analysis is performed for a number of different applications. Absolute and relative relocation [Slunga *et al.*, 1995] are performed using cross-correlation techniques. The SIL algorithm measures travel time differences between each event and all other events in the group, and utilizes the difference to reach very high relative location accuracy (on the order of 5-10 m) and improved absolute location for the group. The method has been used to extensively map active faults in the SISZ and the Tjörnes fracture zone.

New techniques under development for the SIL system include a combination of the information on microearthquake clusters obtained from relative relocation and focal mechanisms in order to monitor fault movement. A cross-correlation method for closely located events is being developed to determine the onsets of P and S phases with higher accuracy, in order to reduce the need for manual inspection of seismograms and to increase the quality of the readings in the microearthquake database. Finally, the stress tensor inversion method described in Paper II and the spectral amplitude correlation in Paper III will eventually be included in the SIL system.

6 Summary of papers

The following sections summarize the four papers upon which this thesis is founded. I will briefly introduce each paper's *raison d'être*, summarize the methods developed and/or data analyzed in the paper and finally give some concluding remarks on the results of the paper. Paper I estimates the crustal state of stress from two deep boreholes in Siljan, Sweden whereas Paper II, III and IV use microearthquakes, recorded by the Icelandic SIL network, to estimate the stress state.

6.1 Paper I

Orientation and magnitude of *in situ* stress to 6.5 km depth in the Baltic Shield

Introduction

In 1994, some five years after the completion of the Gravberg-1 borehole in Siljan, Sweden, there were still Formation MicroScanner data that had not been properly analyzed. I brought the data with me for my stay at Stanford University, and was fortunate enough to be able to work with Prof. Mark Zoback and the Stanford Borehole group in analyzing the FMS, and other Siljan logging data. During their involvement in the Cajon Pass and KTB deep drilling projects, the Stanford group

developed new methods for the estimation of *in situ* stress from wellbore image logs and other borehole measurements. These methods and an associated analysis scheme are referred to as an integrated stress measurement strategy (ISMS), see Section 4. We estimated the orientations of the stresses in Siljan both in the Gravberg-1 and Stenberg-1 boreholes, the magnitude estimates are only from the Gravberg-1 borehole.

Summary

The study started with an estimation of the direction of the *in situ* stresses. For the analysis we utilized borehole breakouts, as recorded both by a 4-arm caliper tool and the FMS tool, and drilling-induced tensile fractures recorded by the FMS tool. Since the traces of all drilling-induced tensile fractures are approximately parallel to the borehole axis and since the borehole is nearly vertical to 4.5 km depth, we conclude that the vertical stress is a principal stress at least to this depth. The directions of the horizontal stresses are estimated from breakouts and induced tensile fractures. We only include data down to 4850 m in the Gravberg-1 borehole and to 5950 m in the Stenberg-1 borehole for the direction estimates. Below these depths the boreholes are deviated more than 15° from the vertical and the directions around the wellbore where breakouts and tensile fractures form depend on the borehole deviation, deviation direction and rock strength properties. We did not have sufficient data to do a proper analysis of rock strength. The mean direction of the maximum horizontal stress, S_H , in Gravberg-1 was estimated to $N72^\circ W \pm 7^\circ$, using circular statistics for the standard deviation. In Stenberg-1 the direction of S_H was estimated to $N53^\circ W \pm 9^\circ$. Although the two boreholes are only 10 km apart, our results indicate that the mean stress directions are not within one standard deviation of each other. The direction of S_H is not constant in the boreholes but show both long and short term variations, some of the short term variations are interpreted as resulting from slip on active faults.

Pore pressure in Gravberg-1 was estimated from three drill-stem tests which indicated hydrostatic pore pressure in the borehole, see Figure 16. The drill fluid pressure was continuously measured during drilling. The vertical stress was calculated from a density profile obtained from a combination of borehole density logs and surface gravity modeling. The magnitude of the least horizontal stress, S_h , was estimated from two drill fluid losses below 6 km and a fracturing operation after the completion of drilling. The errors on these estimates are large, see Figure 16, due to uncertainties in exact depth and the weight of the drill fluid. In addition, there were a number of formation integrity tests performed below the casing shoes at 1250 m and 4167 m, Figure 16. None of these fractured the formation but provide lower limits on the S_h magnitude. We see that the minimum horizontal stress is consistently lower than the vertical stress, with the S_h/S_V ratio being 0.68 at 5 km depth.

Due to limitations in data availability and quality in the Gravberg-1 borehole

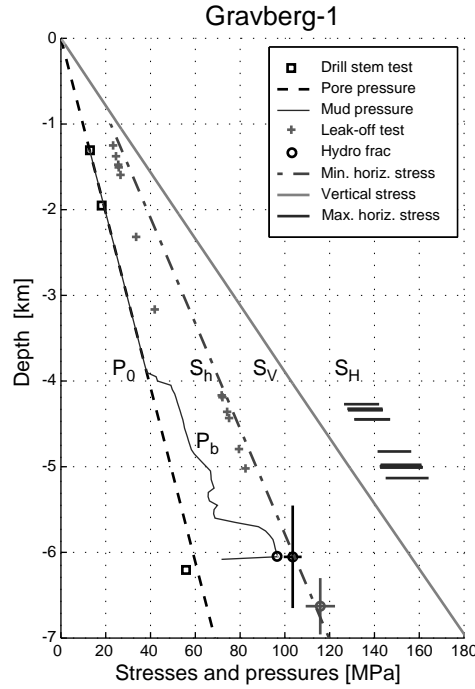


Figure 16: Pore pressure, P_0 , drill fluid pressure, P_b , minimum horizontal stress, S_h , vertical stress, S_V , and maximum horizontal stress, S_H , in the Gravberg-1 well. For the pore pressure there are three data points from the well, open squares, we have then assumed hydrostatic pressure. The drill fluid pressure was continuously measured during drilling. The minimum horizontal stress has been estimated from leak-off tests, pluses, and hydrofracs, open circles. The vertical stress was calculated from borehole density logs and surface gravity modeling. The maximum horizontal stress estimates from induced tensile fractures are shown as horizontal lines, ranging from the lower bound of measured differential pressure, ΔP , and a temperature difference, ΔT , of 10°C to an upper limit where $\Delta P = \Delta T = 0$. We have only included S_H estimates in the depth interval where S_h is best constrained. The figure shows a strike-slip faulting regime.

we could not estimate the magnitude of S_H from borehole breakouts. Instead, we utilized the drilling-induced tensile fractures, using the methodology outlined in Section 4.3. Most of the induced tensile fractures identified in the Gravberg-1 well occurred in zones of natural fractures, hence, we included the pore pressure in our estimates of S_H . This is in contrast to the situation in KTB, where the fractures mostly occurred in unfractured sections of the borehole. The magnitude of S_H is affected by the magnitude of the least horizontal stress, the differential pressure between the drill fluid and the pore pressure in the formation, and the thermal stress. We investigated the thermal stress in some detail, see Equation 74, using the

information on the lithology in the borehole and the temperature dependence of the thermal expansion coefficient to estimate the variations of the thermal expansion coefficient with depth. Using the estimates of S_h from above we will only be able to calculate a lower limit on S_H . This lower limit will depend on the temperature difference between the undisturbed formation and the drill fluid, which affects the thermal stress contribution, and the differential pressure. In Figure 16 we plot magnitudes of S_H in depth intervals where we found induced tensile fractures and where the S_h magnitudes are most well constrained. The lower S_H end is for $\Delta T = 10^\circ$ and ΔP equals the measured differential pressure. The high end of the S_H estimate corresponds to $\Delta T = \Delta P = 0$, i.e. the tensile fractures form even if there is no temperature or pressure difference. The ratio S_H/S_V is estimated to 1.1 at 5 km depth, see Figure 16, i.e. we estimate a strike-slip state of stress at depth in the Gravberg-1 deep borehole. Plotting the maximum and minimum principal stresses in a Mohr diagram indicates that the stress state at Gravberg-1 is controlled by frictional equilibrium on pre-existing faults oriented optimally in the stress field, with a lower bound coefficient of friction of approximately 0.5.

Concluding remarks

The 2-pad FMS tool used in the Gravberg-1 borehole gives rather poor coverage of the borehole wall. In the section of the borehole where we have most FMS data, the diameter of the hole is 21.6 cm, which implies that the two pads of the FMS tool covers approximately 20% of the borehole wall. Frequently one of the images is blurred since the pad has ridden in a breakout and, thus, had poor contact with the wellbore. In such situations it is difficult to assess whether or not a fracture seen on one image is continuous around the wellbore or not. We have been very conservative in our identification of drilling-induced tensile fractures and only included well defined fracture traces.

The integrated stress measurement strategy attempts to include as much stress related information as possible in the estimation of the state of stress. This is especially important in deep boreholes where the individual measurement methods might produce uncertain results but when taken together, these results may reasonably well constrain the state of stress .

6.2 Paper II

Stress tensor inversion using detailed microearthquake information and stability constraints: Application to Ölfus in southwest Iceland

Introduction

In 1996 the Uppsala SIL group started its participation in the European Union project ambitiously referred to as PRENLAB, Earthquake Prediction Research in a Natural Laboratory. As my involvement in the Siljan project was coming

to an end, and as one of the tasks of the Uppsala group in PRENLAB was stress estimation from microearthquake focal mechanisms, I was more than happy to join them. Ragnar Slunga had in 1988 developed a stress tensor inversion algorithm based on the *Gephart and Forsyth* [1984] formulation of the inverse problem, with a new approach to choosing the fault plane and a novel procedure for including uncertainties on the focal mechanism through the inclusion of acceptable focal mechanisms (Section 3.3). We continued development of the algorithm, I rewrote the code for increased efficiency and the inversion scheme was tested and put to work in the SIL environment.

Summary

The basis of stress tensor inversion from earthquake focal mechanisms was reviewed in Section 3.4. Our inversion scheme is based on the grid search method of *Gephart and Forsyth* [1984], although the final formulation is slightly different. We utilize the one-norm measure of misfit but only consider rotations in the fault plane, i.e. we use the pole rotation method in *Gephart and Forsyth* [1984] terminology. Errors in the focal mechanisms are accounted for in a manner that does not require the exact method of *Gephart and Forsyth* [1984]. In order not to under-estimate the size of the confidence limits, we follow *Magee* [1997] and assign both nodal plane normals to 10° bins over the lower hemisphere and then use half the number of filled bins as our number of “non-redundant” data. This number is only used for the confidence limit calculation, we use all data for the inversion. In Paper III the issue of redundancy in the focal mechanism data is further investigated.

The selection of the fault plane from the two nodal planes was discussed in Section 3.4. In our inversion scheme we implemented three alternative techniques for the selection. We use the common slip angle criterion (SA), i.e. choosing the nodal plane with smallest misfit in the tested stress field, for comparison both with other inversion methods and with our other fault selection methods. The new selection criterion introduced in Paper II is based on the notion that the nodal plane that is most unstable in the tested stress field is the plane that slips. Based on a simple Mohr-Coulomb failure criterion we define the instability, I , of a nodal plane as

$$I = \tau - \mu\sigma_n \quad (76)$$

where τ is the magnitude of the shear stress on the nodal plane, σ_n the normal stress on the plane and μ the coefficient of friction. In order to calculate the instability we need to know the magnitudes of the principal stresses. Fortunately, we are only interested in which of the two nodal planes has the highest value of instability, and since we know from Section 2.6 that the relative position of the nodal planes in a Mohr diagram only depends on their orientation with respect to the stress axis, we can unambiguously decide which nodal plane is the most unstable for every value of the coefficient of friction. The coefficient of friction is

usually not well known in the seismic zones and we see from the definition of instability that with varying μ the unstable nodal plane might become the stable nodal plane. We show that the value of μ at the point of cross-over, μ_x , is independent of the magnitudes of the principal stresses, and can be determined from R and the orientations of the nodal plane normals with respect to the principal stress axis and R . During the fault selection process in the inversion we calculate μ_x and if it is outside the range $0.4 \leq \mu \leq 1.5$, which covers friction coefficients for most rock types above 100 MPa [Byerlee, 1978], we select the most unstable nodal plane. If μ_x is within the range, we instead utilize the slip angle criterion. We want to emphasize that the instability (IS) criterion is only used to choose fault plane, it is not used as a misfit criterion. The IS criterion is only valid in areas where fractures in the crust have frictional properties independent of their orientation, in areas dominated by weak faults with a specific orientation the criterion is likely to fail.

As our third fault selection criterion we are able to include information from high accuracy relative relocations [Slunga *et al.*, 1995] produced by the SIL system. If a group of relocated microearthquakes define a common fault plane, and the plane agrees with the events focal mechanisms, this common plane is used as the fault plane for the events.

The fault plane selection methods were tested using both synthetic data and geologic fault slip data. Using synthetic data with noise added and testing both single stress fields and mixed stress fields, the IS criterion performs generally slightly better than the SA criterion. We find, however, that the result of synthetic tests highly depends on the input parameters to the focal mechanism generation and, as such, are difficult to interpret. As a more appropriate test we converted the fault slip data of *Angelier* [1979] into focal mechanisms and inverted them for the stress tensor. The IS and SA criterion both yield similar stress estimates, in agreement with *Angelier* [1979], but where the IS criterion picks all the correct fault planes, the SA criterion only selects 20 out of 38 fault planes correctly.

The stress tensor inversion scheme takes advantage of the acceptable focal mechanisms produced by the SIL focal mechanisms algorithm (Section 3.3). The optimal focal mechanism for each event is accompanied by a number of acceptable mechanisms that satisfies the data only slightly less well. We test all these acceptable focal mechanisms for each event at every grid point in the stress inversion. Note that for each acceptable mechanism we apply the fault selection criterion to identify the proper nodal plane. The acceptable mechanisms have an associated amplitude error and these errors are used to weight the mechanisms relative to the optimal mechanism. The acceptable (including the optimal) mechanism which produce the lowest misfit is selected to represent the event in a particular grid point. When the optimal stress tensor has been identified, the inversion scheme has also selected the most appropriate focal mechanism for each event from the acceptable mechanisms.

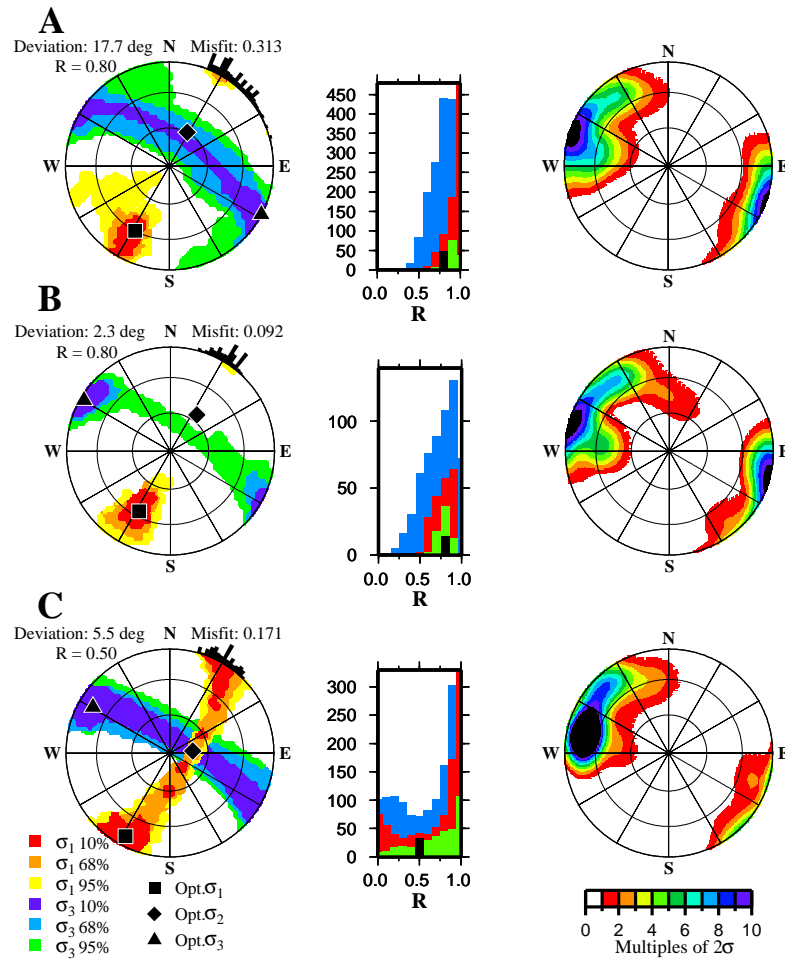


Figure 17: Stress tensor inversion results from Ölfus, Iceland. All inversions have been performed with the instability fault selection criterion. Grids are equal-area projections of the lower hemisphere. To the left are the resulting optimal stress tensors; σ_1 , square, σ_2 , diamond, and σ_3 , triangle; together with the 10%, 68%, and 95% confidence limits for σ_1 , red to yellow from 10% to 95%; and σ_3 , purple to green from 10% to 95%. Deviation is the average angle between the directions of estimated shear stress and observed slip on the planes, misfit is deviation weighted with amplitude errors and R is the optimum R value. The black histogram on the perimeter shows the 95% confidence level for the direction of maximum horizontal stress. In the middle are histograms of the 10%, green, 68%, red, and 95%, blue, confidence limits in R , the black spike is the optimum value. To the right are Kamb contours of the fault plane normals chosen by the inversion. A) Inversion using only the optimal focal mechanism for each event. B) Inversion with all acceptable mechanisms for each event. C) Inversion with 41 events having predefined planes from relocation and using all acceptable mechanisms for the remaining 37 events.

The stress tensor inversion was applied to 78 microearthquakes from a small volume, 1.6 km N–S, 1.3 km E–W and 5.9 km deep, in Ölfus, southwest Iceland. 41 of the events could be assigned a “correct” fault plane from relative relocation. In Figure 17 we show the results of three different inversion using the instability fault selection criterion. Comparing Figures 17A and B, we see how the inclusion of acceptable focal mechanisms significantly reduces the misfit and deviation and also reduces the size of the confidence limits, making the resulting stress state more well constrained. The optimal stress states are approximately the same and the chosen fault planes have approximately the same orientations in both inversions. In Figure 17C we have included predefined fault planes for 41 of the 78 events. The first thing to note is that the chosen fault planes of all three inversions are very similar, i.e. the instability selection criterion is successful in picking the correct fault planes. The state of stress is less well constrained in Figure 17C and we see that the misfit has increased. All three inversions show a rather stable direction of maximum horizontal stress at approximately N30°E.

Stress inversion with the instability selection criterion was compared to inversion using the slip angle criterion. The stress states estimated by using the two different criteria are similar but, when compared to the predefined planes, the slip angle criterion picks the wrong nodal plane for more than 50% of the events.

Concluding remarks

This study showed that a nodal plane selection criterion based on the stability of the planes in the stress field is significantly better at predicting the correct fault planes than a misfit based selection criterion. Including a range of acceptable focal mechanisms for each event constrains the stress estimate better than using a single mechanism per event. The range of mechanisms also lowers the misfit.

Testing the stability selection technique in an area with strongly anisotropic friction conditions, such as close to a large, well established fault, would be very interesting. Preliminary inversions of microearthquake from the Husavik fault region in northern Iceland, showed that the stability criterion very consistently picked the wrong fault planes, as compared to relative relocations. If this is a general pattern, the combination of stress tensor inversion and relative relocation could become useful as a means of assessing the stability of faults in different directions and identifying established faults at depth.

6.3 Paper III

Correlation of microearthquake body-wave spectral amplitudes

Introduction

During the work on Paper II, and especially during the period when I performed synthetic tests on the stress inversion algorithm, we frequently discussed the issue of the similarity of the focal mechanisms we input to the inversion. As I discussed

in Section 3.4.1, the stress tensor inversion needs focal mechanisms sufficiently well distributed in terms of orientation in order to produce well constrained estimates. It is thus important to assess how similar, or redundant, the focal mechanisms are for a group of events before they are input to the inversion. When calculating the confidence limits it is necessary to disregard the redundant events, or the confidence limits will be unrealistically small. In the SIL group, we also discussed the possibility to disregard redundant events altogether in the inversion, only including one event as a representative for a group of similar events, in order to shorten computer run-times. Quantifying the similarity of focal mechanisms in terms of the strike, dip and rake angles is not trivial. In addition, the SIL focal mechanism algorithm [Rögnvaldsson and Slunga, 1993] provides us with, very valuable, information on the uncertainty in the mechanisms in terms of a range of acceptable focal mechanisms. These acceptable mechanisms further complicates the similarity test. A solution to the similarity test problem is spectral amplitude correlation and grouping. We return one step back in the chain of earthquake data processing. The focal mechanisms are calculated from spectral amplitudes and polarities [Rögnvaldsson and Slunga, 1993], so by comparing the spectral amplitude distributions of closely located events, we can assess their similarity in terms of focal mechanisms.

Summary

The SIL system calculates spectral amplitudes on three component data rotated into vertical, radial and transverse components. Windows are placed on the direct P and S wave arrivals and transforming to the frequency domain the low frequency asymptotes, or DC-level spectral amplitudes, are estimated for the different components [Rögnvaldsson and Slunga, 1993]. We obtain five amplitude values at each recording station; vertical and radial P (PZ and PR) and vertical, radial and transverse S (SZ, SR and ST), which we refer to as amplitude components. These amplitude components, together with first motion directions, form the basis for the focal mechanism calculation in the SIL system and will be utilized in the spectral amplitude correlation and grouping scheme.

In order to assess the similarity of the focal mechanisms of two different events all amplitude components in common for the two events are correlated using linear cross-correlation

$$r = \frac{\sum_i (x_i - \bar{x})(y_i - \bar{y})}{\sqrt{\sum_i (x_i - \bar{x})^2} \sqrt{\sum_i (y_i - \bar{y})^2}} \quad (77)$$

where r is the correlation coefficient, \bar{x} is the mean of the logarithms of one event's amplitude components, x_i , and \bar{y} the mean of the logarithms of the other event's amplitude components, y_i . The logarithms are utilized to decrease the importance of the nearest stations, thereby stabilizing the correlation. We use the correlation coefficient as the measure of how similar two events are.

All events are correlated with all other events and the events are then grouped

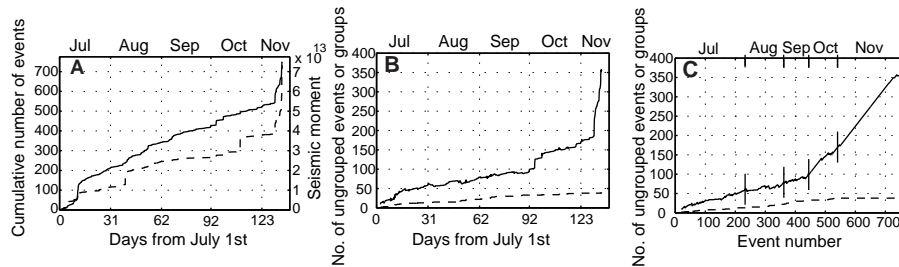


Figure 18: Correlation results at Ölfus, July 1 to November 13, 1998. A) Plotted versus time in days is the cumulative number of events (solid line, scale to the left) and the cumulative scalar seismic moment (dashed line, scale to the right). B) Number of ungrouped events (solid line) and the number of groups (dashed line) versus time in days. C) Number of ungrouped events (solid line) and number of groups (dashed line) versus the event number.

according to the correlation coefficients. The grouping is controlled by three parameters; a lower limit on the correlation coefficients, r_{min} , a lower limit on the fraction, f_{min} , of fellow events in the group that a single event is allowed to have below r_{min} and the minimum number of events needed to have a group. After some testing we adopted $r_{min} = 0.9$, $f_{min} = 0.8$ and at least four events in the group, as our parameters for studying larger amounts of seismicity. If a more detailed study on fewer events is desired, the r_{min} and/or f_{min} values should be increased. We define two modes of running the correlation and grouping, the first correlates all events in a catalogue with all other events in one large run, and then performs an iterative grouping that allow us to find the optimal homogeneity within the groups. The second mode starts with a small group of events that are correlated and grouped, and then the events are correlated and grouped one by one with the previous events. This mode will not obtain the optimal group homogeneity but instead it allows us to study the time variations in correlation and grouping.

During the development of the correlation and grouping scheme we discovered that it is useful also for applications other than as a preprocessor to stress tensor inversion. If we run the correlation in the second mode the temporal evolution of the earthquake grouping patterns can be studied and the groups of similar events produced by the grouping can be utilized either for composite focal mechanism calculations or as a starting group for relative relocation. We tested the correlation and grouping algorithm on a set of 636 microearthquakes, $0.0 \leq M_L \leq 2.7$, occurring between July 1, 1998 and November 13, 1998 in Ölfus, southwestern Iceland. On November 13 there was a magnitude 5.0 earthquake in the Ölfus area. Cumulative number of events and cumulative seismic moment is plotted in Figure 18.

Studying the Ölfus seismicity using the second mode of correlation and group-

ing we obtain the plots in Figure 18B and C. In Figure 18B we see that the seismicity in July correlate very well, the rapid increase in number of events is not mirrored by an increase in the number of ungrouped events. Conversely, the increase in seismicity in November has an associated increase in the number of ungrouped events. The grouping pattern becomes clearer if we plot the number of ungrouped events and number of groups as a function of the event number, Figure 18C. We now clearly see a change in the grouping pattern around event 430, which corresponds to late September, where the slope of the curve significantly changes. We interpret the lack of correlation after September as an indication that the microseismicity changed characteristics. Before late September many events occur on the same fault (or a very close, similarly oriented fault) with very similar slip directions. We refer to these events as *repeated* events. After September, spectral amplitude correlation indicates that either the focal mechanisms are different, both compared to earlier and to current seismicity, or the events occur at different locations compared to earlier and current seismicity. These events will be referred to as *solitary* events. High accuracy relative relocation [Slunga *et al.*, 1995] supports the notion of a more diffuse seismicity towards the end of the period.

Using one of the groups produced by spectral amplitude correlation of the entire data set, now with $r_{min} = 0.9$ and $f_{min} = 0.9$, we compute a composite focal mechanism. There were 27 events in the group and the nodal planes of the optimal focal mechanisms have a spread of approximately 50° , both in strike and dip. Utilizing the spectral amplitudes from the 27 events we compute a median distribution of spectral amplitudes for the entire group. All events' first motion directions are stacked and then the combined amplitudes and polarities are used to compute a new focal mechanism using the SIL algorithm. The nodal planes of the composite focal mechanism are compared to the result of relative relocation, and one of the nodal planes is only 15° away from the common fault plane defined by the relocations. The fit is not perfect, but considering the rough amplitude stacking technique it is quite good. Among the acceptable focal mechanisms we find one nodal plane that is only 7° away from the common fault plane.

Finally, we test the correlation and grouping scheme in terms of input to the stress tensor inversion. Magee [1997] discussed the issue of redundant focal mechanisms and approached the problem by assigning the nodal plane normals to 10° bins over the lower hemisphere and using half the number of filled bins as the number of non-redundant events when calculating the confidence limits. The correlation and grouping scheme can be used to assess the similarity of closely located events, i.e. if two events have identical focal mechanisms but are far from each other (depending on station geometry and focal mechanism), they will not be identified as similar. The correlation will, thus, not be able to identify all redundant focal mechanisms, but as we shall see below, it can significantly improve the calculation of confidence limits and reduce the size of the data set. We will use the term *reduced* events instead of non-redundant henceforth.

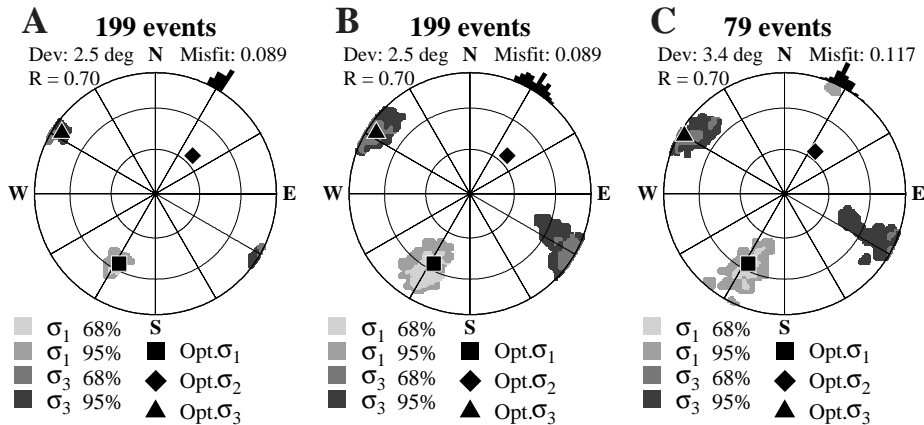


Figure 19: Stress tensor inversion of the 199 events from Ölfus, Iceland, July, 1998. Symbols and patterns are as in Figure 17, with the exception that I do not plot the 10% confidence limits for the stresses here. A) Inversion result using 199 events and 199 as the number of events when calculating the confidence levels. B) Result using 199 events in the inversion and 59 reduced events, according to *Magee* [1997], for the confidence level calculation. C) Result using 79 reduced (from spectral amplitude correlation) events, of which 10 are composite events, for both the inversion and the confidence level estimates.

We perform stress tensor inversions using both the full number of events and the binned number of events for calculating confidence limits and compare these to an inversion of a data set reduced by the correlation. Microearthquake data from 1998, 199 events in July and 182 in November, is used for the inversions. I show here the result of the July data. The binning technique of *Magee* [1997] estimates that there are 59 reduced events in July and the spectral amplitude correlation results in 69 ungrouped events and 10 groups, i.e. 79 reduced events. In Figure 19 we show the inversion results using the three different approaches and the inversion algorithm of Paper II. Figures 19A and 19B show the confidence regions obtained using 199 and 59 reduced events, respectively, to calculate the confidence limits. The inversion itself uses all 199 events which is shown by the identical misfits and optimal stress states. We see that there is a large difference in the size of the confidence areas. In Figure 19C is the result of using spectral amplitude correlation to estimate the number of reduced events and using only the reduced events in the inversion. Running the July inversion with the 79 reduced events instead of 199 significantly shortens the necessary computer time. We see in Figure 19C that the optimal stress state is almost identical to the state estimated using the full data set but that the misfit is slightly larger when using only 79 events in the inversion. This is not surprising since among the 199 events there are most likely some rather poorly constrained mechanisms, resulting in a large

number of acceptable focal mechanisms which gives the inversion algorithm larger freedom in the choice of fault plane, see Paper II, compared to using 79 well determined events.

Concluding remarks

The spectral amplitude correlation and grouping technique has proven a successful method in terms of assessing the similarity of focal mechanisms of closely located events and grouping of similar events. An event representing the group is selected either through a composite focal mechanism or by choosing the highest quality event, i.e. the event with most stations, amplitude components and polarities. The grouping technique also allows us to form batches of a certain number of reduced events, which will be useful in studies of temporal or spatial variations in the stress field, as in Paper IV.

The issue of how different the focal mechanisms have to be in order to be considered non-redundant in the inversion has not been meticulously studied. We observed the grouping patterns and empirically found values of the grouping parameters that produced homogeneous groups, minimizing the number of events that “almost” made it into the groups.

In order to study the influence of spatial variation on the grouping result we will implement means of taking the events locations into account.

The spectral amplitude correlation and grouping technique seems to be a very promising tool for the study of temporal or spatial variations in earthquake repeating patterns. By repeating pattern we refer to changes in the number of repeated events (or groups of repeated events) versus the number of solitary events. A larger study of microearthquake repeating patterns will be undertaken in Paper IV.

6.4 Paper IV

Spectral amplitude grouping and the state of stress: A study of microearthquake activity before the November 13, 1998, magnitude 5.0 earthquake in Ölfus, Iceland

Introduction

The sequel to PRENLAB is PRENLAB-2, and the Uppsala SIL group continued its participation in the project. Remembering that PRENLAB is an earthquake prediction research project, it was obvious to us that the methods developed in Paper II and III should be applied to a study of microearthquakes *before* a larger earthquake. We chose the November 13, 1998, $M_L = 5.0$ earthquake in Ölfus, southwestern Iceland, and studied the seismicity one year prior to the main event.

Summary

We analyzed microearthquakes occurring in the Ölfus area between November 1, 1997 and November 13, 1998, seven hours after the main shock. All events with at least four recording stations, 18 amplitude components, one polarity reading and $M_L \geq 0$ were included in the study, resulting in a catalogue of 2943 events. Using relative relocations we know that the main event, a right-lateral strike-slip event, took place on a N–S striking fault and that many of the events in our study also occurred on N–S striking faults.

In this paper we decided to use the name *Spectral Amplitude Grouping* (SAG) for the correlation and grouping technique developed in Paper III. We also split the second mode of operation from Paper III into two, where mode 2 is equivalent to the second mode above but where mode 3 now is the mode used to produce batches of a predetermined number of reduced events. The mode 2 of SAG has in this paper also been further developed to accommodate a variable size of the correlation memory. In Paper II, all events were retained in the correlation memory implying that early events were correlated with very few events and later events were correlated with almost the entire event catalogue. Now it is possible to choose the number of events to retain in the correlation memory, i.e. SAG can act as a moving window filter.

In order to study the repeating pattern of the Ölfus seismicity, and test the influence of the length of the correlation window, we ran SAG twice on the Ölfus data, see Figure 20. In the first run, in Figures 20A and B, we retained all events in the correlation memory. Figure 20A indicates that there is a steady increase in the number of solitary events with time, until we reach November and the foreshocks to the main event, when the number of solitary events increase rapidly. What is less noticeable is the rapid increase in the number of groups at Eq1, where there is a large number of aftershocks occurring as the result of a $M_L = 5.1$ earthquake to the north of the study area. We, hence, have two different responses to an increase in seismicity, in June the aftershocks are almost all repeating events that group very well, whereas the November foreshocks are mostly solitary events. The repeating pattern becomes clearer, we avoid the influence of the seismicity rate, if the number of solitary events is plotted versus event number, Figure 20B. We now have a more detailed view, the number of solitary events first increase until mid March, where the increase rate levels off. In June the rate is almost flat, most of the seismicity consists of repeated events, and then, in late August, early September, the rate of the number of solitary events increases dramatically. There is some decrease in the rate after the November event but it is not until further into the aftershocks that the rate of solitary events decreases substantially. How is this repeating pattern affected by the size of the correlation memory? In Figures 20C and D are the results of a 250 event correlation memory. Note that the first 250 events should not be included in the analysis since we are filling up the correlation memory and the solitary event rate will be high. The large scale pattern is generally the same, but we see that we have substantially increased the time resolution.

Decreases in the number of solitary events are caused by two mechanisms; new events correlating well with older, solitary, events and old, solitary events leaving the correlation memory. Figure 20D shows that the seismicity after mid-March are repeating events and that there is a small increase in the number of solitary events immediately after the June main event but that the aftershocks soon are very similar. With this resolution we also note that the onset of a different type of seismicity occurs already in July and that the the number of solitary events peaks on the main November event. There is a small trough immediately before the main November event, as if the seismicity settled into a repeating pattern

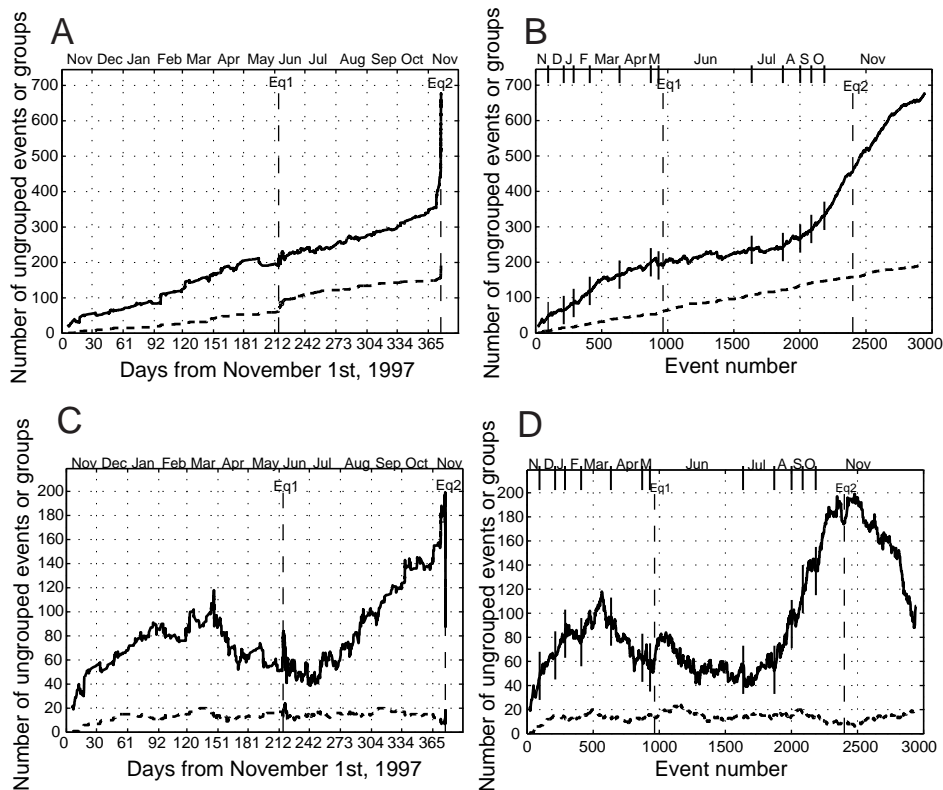


Figure 20: Spectral amplitude grouping (SAG) results, or repeating patterns, for the Ölfus seismicity. Eq1 is the $M_L = 5.1$ event north of the study area, Eq2 is the main November event. A) The entire catalogue is used as correlation memory. Number of solitary events (solid line) and number of groups (dashed line) versus time. B) Same as in A but now plotted versus the number of processed events. C) Using a 250 event moving window as correlation memory. Number of solitary events (solid line) and number of groups (dashed line) versus time. D) Same as in C but now plotted versus the number of processed events. In B and D the start of each month is indicated by short, solid lines down from the top of the frames.

before the main event occurred. After the main event there is a short increase in the number of solitary events and then the aftershocks seem to localize, or stabilize, and become repeating events. Using a 100 event correlation memory produces approximately the same pattern, including the trough at the November event, whereas a 500 event memory seems a little too long and does not decrease as quickly after the main event as do the shorter memory sizes.

Using the spectral amplitude grouping technique in mode 3 we produced 76 batches of 40 reduced events for stress tensor inversion. The batches overlap by 20 reduced events. We also ran SAG in mode 1 on a data set where the aftershocks to the June event and the fore- and aftershocks to the November event were taken out, producing a list of 438 reduced events for the year. The list was used to estimate the background state of stress for the studied year.

The background stress state was estimated to an oblique strike-slip state with a normal faulting component. The least principal stress, σ_3 , is subhorizontal in the direction N51°W, in agreement with the N63°W direction of spreading across south Iceland [*Sigmundsson et al.*, 1995]. The maximum horizontal stress is in the direction N36°E. The stress state is very well constrained with small confidence areas and, surprisingly, we find that none of the principal stresses are vertical.

We estimated one stress state for each of the 76 batches of reduced events and in Figure 21 we show, as an example of the results, the direction of maximum horizontal stress, A and B, and the magnitude of the maximum horizontal stress relative to the vertical stress, C and D. The first order impression of the direction of maximum horizontal stress, σ_H , is a rather stable direction around N30°E, with a 68% confidence limit of 30° – 40°, during the year. There are some batches that have a deviation which is significant at the 68% level with respect to other batches, such as batch 52 with respect to batch 11, 22, 66 and 69. There are temporal variations in the confidence limit, which is sometimes very well constrained and sometimes very large, indicating perhaps inhomogeneity in the stress field. There is some indication of a rotation in the horizontal stress towards N–S around November 9. Assuming a coefficient of friction of $\mu = 0.6$, hydrostatic pore pressure and a vertical stress that equals the weight of the overburden, we can estimate the magnitudes of the maximum horizontal stress. These magnitudes may be incorrect, but the pattern of magnitudes relative each other is constant. We see in Figure 21 that there is no systematic variation in the horizontal stress magnitudes but that there are indications of variations. Most pronounced is the group of four batches in July and the rather well constrained decrease after the mainshock in November.

We studied the sizes of the 68% confidence limit areas and the differences in deviation angle between the chosen and the rejected nodal planes from the stress inversions. We also separated the data set into two sets, group 2 containing the area of most intense aftershocks activity from the June event, and group 1 with the remaining events. The SAG of group 1 show the same repeating patterns

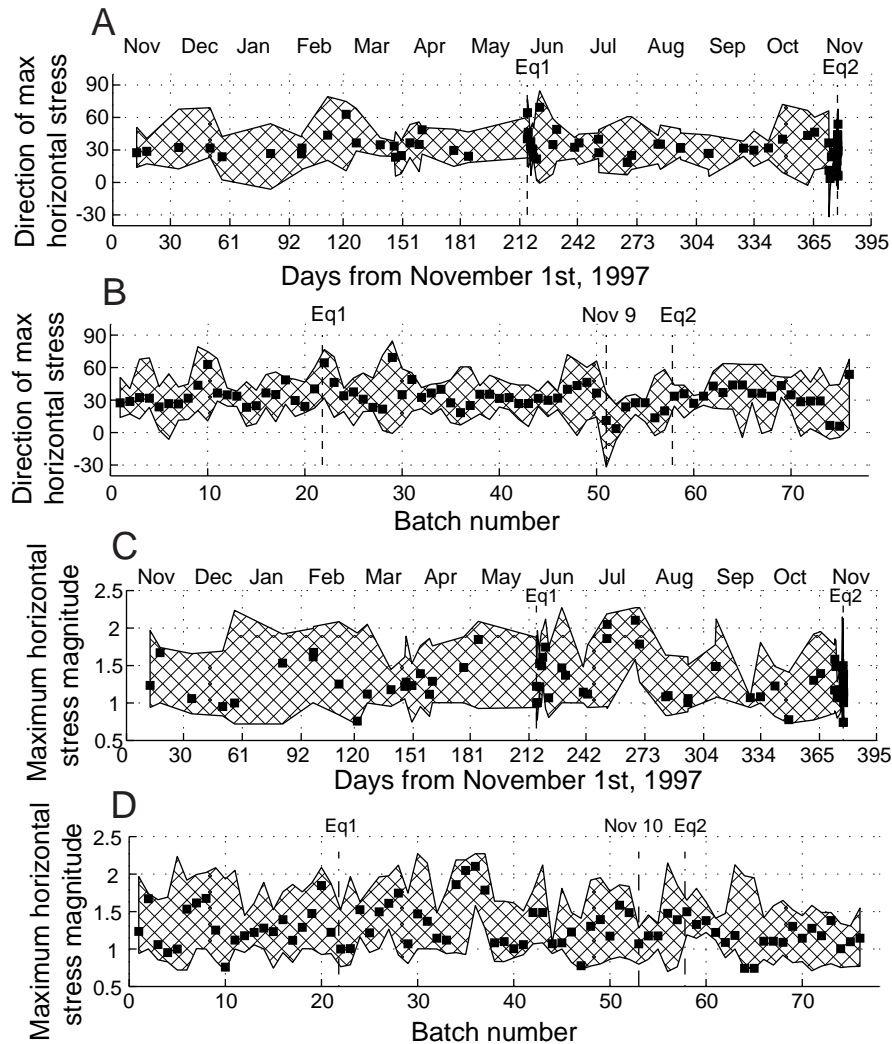


Figure 21: Results of stress tensor inversions of batches of 40 reduced events. Eq1 is the time of the June 5.1 event, Eq2 is the November 5.0 event. Solid squares are the optimum solutions for each batch and the hatched band is the 68% confidence limits. A) Directions of maximum horizontal stress in degrees east of north versus time. B) Same as in A but plotted against the batch number for clarity. C) Variation of the magnitude of the maximum horizontal stress during the studied time period. In order to estimate the stress magnitudes we used a coefficient of friction $\mu = 0.6$, hydrostatic pore pressure and normalized the magnitudes to the weight of the overburden. D) Same as in C but plotted against the batch number.

as in Figure 20, but without the June peak. In group 2 the June pattern again shows how similar the events are. Stress inversion of batches of 40 events show an interesting feature. The June aftershock seismicity seems to be influenced by

a more NE–SW trending maximum horizontal stress. The inversions of group 1 events show that the stress states are generally more well constrained than for the entire data set. There is, again, an indication of a rotation of the direction of maximum horizontal stress from N–S towards NE–SW around the main event.

Concluding remarks

The spectral amplitude grouping results are very interesting and show that SAG in mode 2 can provide a new view of the temporal evolution of seismicity. Further, the large anomaly in the latter part of the study seems to be associated with the main November event. This opens up interesting prospects of SAG as a monitoring instrument. I will analyze a longer series of events from the Ölfus area in order to obtain more information on the normal variations in repeating patterns.

There seems to be very little correlation between the repeating pattern from SAG and the estimated stress states. I have not performed any rigorous significance tests on the fluctuations in e.g. the direction of maximum horizontal stress, so I am uncertain of the significance of the variations observed.

7 Concluding reflexions

In this thesis I have presented a variety of methods and approaches for the estimation of the state of stress in the crust. This variety, in itself, points to one of the conclusions of the thesis. Crustal stresses are inherently difficult to measure, and well constrained estimates of the crustal stress tensor are only rarely obtained. The difficulty of direct measurements of stress at depth has led to a flora of indirect measurement techniques, with associated estimation procedures, of which I have presented a few in this thesis.

The analysis of the state of stress in Gravberg-1, using measurements from the deep borehole, serves as a good example of the difficulties involved in measuring stresses at depth. Formation integrity tests, losses of drill fluid circulation, measurements of the geometry of the borehole and images of 20% of the borehole wall from 25% of the length of the borehole; one by one these observations tell us very little about the stress state. Taken together however, in a joint analysis scheme such as the integrated stress measurement strategy discussed in the thesis, these pieces of information can be assembled to a relatively reliable estimate of the state of stress. We find that there is a strike-slip stress regime at depth in Siljan and we estimate the horizontal deviatoric stress, $S_H - S_h$, to approximately 60 MPa at 5 km depth. We infer that the state of stress is controlled by frictional equilibrium on pre-existing faults, oriented optimally in the stress field, with a lower bound coefficient of friction of 0.5. Integrating all available information can thus yield significantly more information than what is obtainable from the individual methods.

Estimating the state of stress from earthquake focal mechanisms adds another level of difficulty. The geometric information contained in the focal mechanisms does not allow an estimation of the magnitudes of the stresses, neither the absolute principal stress magnitudes nor the magnitude of the maximum shear stress. The principal stress orientations and the ratio $R = (\sigma_1 - \sigma_2)/(\sigma_1 - \sigma_3)$ are obtained from the inversion of focal mechanisms, magnitudes can only be calculated with additional information on the coefficient of friction, the pore pressure and the vertical stress.

In this thesis I have addressed three aspects of stress tensor inversion using earthquake focal mechanisms; the ambiguity in the selection of the fault plane from the two nodal planes, the inclusion of uncertainties in the focal mechanisms and the assessment of focal mechanisms in terms of redundant information. All testing and application of the developed methods have been to microearthquakes recorded by the SIL network in southwest Iceland.

Previous work has shown that selecting the correct fault plane from the two nodal planes does affect the estimated state of stress, but that, especially for larger data sets, the estimated stress tensors can be rather similar. Generally, I consider that selecting the correct fault plane lends more credibility to the inversion results, and if we are studying faulting or the stability of faults, it is necessary to choose the correct fault plane. In this thesis, a fault selection criterion with a physical background is proposed, based on the stability of the two nodal planes in the tested stress field. I simply choose the most unstable fault, if the choice can be made without ambiguity. This criterion proved very successful in the tests I conducted and generally performed better than the more common selection criterion based on least angular misfit.

A focal mechanism is the result of an over-determined inversion scheme where four, or more, parameters are estimated from amplitude and/or polarity data. As with other such estimates, the focal mechanism has some associated uncertainty. We include the uncertainty in the focal mechanisms in the stress inversion via the range of acceptable focal mechanisms available in the SIL system. These acceptable mechanisms do not fit the data as well as the optimal mechanism, but we know that they agree with the bulk of the data. By using them in the inversion, instead of rotating the optimal mechanism within some uncertainty limit, we will not violate the amplitude and polarity data. The range of acceptable focal mechanisms significantly reduces the misfit in the stress tensor inversion.

A large number of earthquakes with very similar focal mechanisms do not constrain the stress tensor inversion more than do one or two earthquakes with the same mechanisms. Instead, a large number of similar events acts to unduly decrease the estimated confidence limits and increase the inversion time. In order to reduce the number of similar focal mechanisms we invented a correlation and grouping technique (SAG) based on spectral amplitudes, the input data for the focal mechanism estimation. SAG allows us to identify closely located microearth-

quakes with similar focal mechanisms and delete these from the input data set to the stress inversion.

The spectral amplitude grouping technique, unintentionally, proved very useful for the assessment of variations in the patterns of repeating microearthquakes. SAG identifies groups of repeating microearthquakes, i.e. closely located events with similar focal mechanisms, and events that are non-similar or have isolated locations, solitary events. The variation in the number of solitary events and the number of groups, in time or space, provides a new view of the seismicity patterns.

The earthquake stress inversion and SAG methods were applied to one year of seismicity before the November 13, 1998, $M_L = 5.0$ event in Ölfus, Iceland. Using a 250 event moving correlation memory, the SAG technique unveils an intricate pattern of solitary and repeated events, with a rapid increase in the number of solitary events during three months before November 13. The number of solitary events peaks at the time of the November 13 earthquake and then decreases as the aftershocks become similar. Inversion for the background stress field shows a very well constrained oblique strike-slip regime with a normal faulting component. The least principal stress is subhorizontal in the direction $N51^\circ W$, which agrees with the direction of spreading in southwest Iceland. The maximum horizontal stress is in the direction $N36^\circ E$. Inverting batches of 40 events, spread over the year, we observe, to first order, a rather stable stress field which contains some variation over the year. There are indications of a rotation to the north of the horizontal stresses some days before the main event, there are also indications of changes in the horizontal stress magnitudes and indications of heterogeneities in the stress field. I have, however, not performed a rigorous statistical investigation of these fluctuations. Even if the stress fluctuations were to be statistically significant, there is in the temporal stress estimates very little correlation with the dramatic variations observed in the results of the spectral amplitude grouping.

This thesis shows that there is significant information to acquire from micro-earthquake activity. The large number of events obtained when we record micro-earthquakes to magnitudes below zero provides us with very valuable information on the ongoing deformation processes. If properly deciphered, this information can potentially teach us much more about earthquake generating crustal processes, processes that, no doubt, influence or are driven by, stress.

Acknowledgments

Returning to Uppsala in the autumn of 1995, after having spent a year in the California sunshine, I found myself in the extraordinary situation of being able to pick and choose from the smorgasbord of geophysical topics available at the department. It did not take very long though, before Reynir had convinced me that whatever I wanted to pursue in geophysics was available from the SIL network and that Iceland harboured more geophysically interesting problems than the rest of the world put together. What more is there to say? I joined the party and was awarded with two advisors, Ragnar Slunga and Reynir Böðvarsson. Working with these two skilled and creative scientists, not to mention incurable optimists, has been an adventure. Reynir was of course right about the problems, I ran my head into quite a few of them, but with Ragnar's words of wisdom and Reynir's helping hand, I managed to pound my way through.

I spent a couple of months of my studies in Iceland, at the Icelandic Meteorological Office in Reykjavik and at Hitaveita Akureyrar in Akureyri. Coming to work at the Met Office was always very productive and working with Sigurður Rögnvaldsson was fun and educating. He was my big brother in SIL, teaching me the inner workings of the SIL system and interpreting the native tongue. Many thanks also to Nanna for the halibut dinners! Kristjan Ágústsson, Ragnar Stéfansson and the rest of SIL crew, thanks for having me around. The yearly excursions with the amateur glaciologists and Richard, Ásta and Halla were lots of fun.

Back at the department in Uppsala, Christopher Juhlin answered endless questions about the Siljan drilling operations and thoroughly reviewed both my first and second paper. Many thanks for the commas, Chris! Laust B. Pedersen guided my first steps into geophysics, showed me the intricacies of tellerrestrial electromagnetics and sent me off to Stanford with the Siljan FMS tapes. A job well done, and thanks for letting me stray off into seismology when I got home! Thanks also to Laust and Roland Roberts, who scrutinized the summary part of this thesis. For scientific discussions, and not so scientific discussions, I thank all the teachers and researchers at the department! Conny Holmqvist and I spent some memorable moments together in the Kurravaara winter, I'm still thawing my toes. Hasse Palm and Lars Dynesius started teaching me how to do seismic reflection field work, but gave up on me when I showed affections for passive sources.

What would you do without fellow students? Probably, you would finish in half the time and with a much cleaner vocabulary! But, what fun would that have been? Thanks guys! Siggí, Are and Nikke for showing me the real reason why lunch at Stockholms is soooo much better than elsewhere. Johannes, Niklas and Lena, for educating me by always having another question. Skånepågarna for convincing me that Roskilde 1658 was a major mistake (although a bottle of Glenlivet does make up for a lot, Stefan). Puy for an endless fountain of optimism and who, together with Los Amigos de Centro America, tried to keep up my Spanish. The

Persians for help and friendship, Sverker for taking over all my responsibilities (have fun!) and my old students; Lill-Björn, Kattis, the Gun, Matilda and the rest, for the nerve-wrecking introduction to teaching.

The 13 months I spent at Stanford University did wonders for my knowledge of geophysics. Do you know there's a world out there?! Thanks to the Fulbright Commission for the grant, to Simon Klemperer for taking me on and to Mark Zoback for getting me out on the other end. Special thanks to Mark for teaching me how to write a paper, "I like your data analysis Björn, but the paper is a near complete disaster.", followed by pages of good advice. Big thanks to my friends in the seismic group, the borehole group and all the guys who started when I did. Special "Hei" to Per for the late night visits to the coffee shop. Shirin Ahlbäck and Maria Holmgren-Troy appeared one day on a Fulbright pass, full of enthusiasm and energy which was just what I needed at that time, thanks! Pete Brownell and the Biorockhuggers, what can I say? No matter what the geologists think, a good granite is a vertical granite! Thanks for taking me to the Valley and thanks for hanging on!

Fysik-kemisterna, thanks for showing the way. You made it look so easy!

There are friends, and then there are friends. I am very happy that they did not teach chemistry at the gymnasium in Katrineholm! Thanks for cheering me on Danne and for friendship and hospitality from you and Helena over the years.

Encouragement, support and a gentle kick in the behind. That's what family is for. You did it, it finally looks like I'm going to finish school! Thanks everybody for bedtime stories and homes away from home. Thanks Elisabeth and Carina for being sisters.

Two geophysics PhDs in the family. This could mean a down to earth life style but considering your involvement with explosion seismics, hmmm, I don't know. I thought the joint thesis writing could get tough, but you even enjoyed it! Thanks for being here Lena.

References

- Aki, K. and P. G. Richards, *Quantitative seismology, theory and methods*, W. H. Freeman, San Francisco, 1980.
- Allen, R. *et al.*, The thin hot plume beneath Iceland, *Geophys. J. Int.*, *137*, 51–63, 1999.
- Amadei, B. and O. Stephansson, *Rock stress and its measurement*, Chapman and Hall, London, 1997.
- Angelier, J., Determination of the mean principal directions of stresses for a given fault population, *Tectonophysics*, *56*, T17–T26, 1979.
- Angelier, J., Tectonic analysis of fault slip data sets, *J. Geophys. Res.*, *89*, 5835–5848, 1984.
- Angelier, J., Inversion of field data in fault tectonics to obtain the regional stress, III. A new rapid direct inversion method by analytical means, *Geophys. J. Int.*, *103*, 363–376, 1990.
- Angelier, J., A. Tarantola, B. Valette, and S. Manoussis, Inversion of field data in fault tectonics to obtain the regional stress, I, Single phase fault populations: A new method of computing the stress tensor, *Geophys. J. R. Astron. Soc.*, *69*, 607–621, 1982.
- Armijo, R., E. Carey, and A. Cisternas, The inverse problem in microtectonics and the separation of tectonic phases, *Tectonophysics*, *82*, 145–160, 1982.
- Barton, C., M. D. Zoback, and K. Burns, In-situ stress orientation and magnitude at the Fenton Hill geothermal site, New Mexico, determined from wellbore breakouts, *Geophys. Res. Lett.*, *15*, 467–470, 1988.
- Bell, J. and D. Gough, Northeast–southwest compressive stress in Alberta: Evidence from oil wells, *Earth Planet. Sci. Lett.*, *45*, 475–482, 1979.
- Bergerat, F., Á. Guðmundsson, J. Angelier, and S. T. Rögnvaldsson, Seismotectonics of the central part of the South Iceland Seismic Zone, *Tectonophysics*, *298*, 319–335, 1998.
- Bjarnason, B., C. Ljunggren, and O. Stephansson, New developments in hydrofracturing stress measurements at Luleå University of Technology, *Int. J. Rock. Mech. Min. Sci.*, *26*, 579–586, 1989.
- Bott, M. H. P., The mechanics of oblique slip faulting, *Geol. Mag.*, *96*, 109–117, 1959.
- Böðvarsson, R., S. T. Rögnvaldsson, S. S. Jakobsdóttir, R. Slunga, and R. Stefánsson, The SIL data acquisition and monitoring system, *Seismol. Res. Lett.*, *67*, 35–46, 1996.
- Böðvarsson, R., S. T. Rögnvaldsson, R. Slunga, and E. Kjartansson, The SIL data acquisition system — at present and beyond year 2000, *Phys. Earth Planet. Inter.*, *113*, 89–101, 1999.
- Bredehoeft, J., R. Wolff, W. Keyes, and E. Schuter, Hydraulic fracturing to determine the regional in situ stress field, Piceance Basin, Colorado, *Bull. Geol. Soc. Am.*, *87*, 250–258, 1976.
- Brudy, M., *Determination of in-situ stress magnitude and orientation to 9 km depth at the KTB site*, Ph.D. thesis, Universität Karlsruhe, Karlsruhe, Germany, 1995.
- Brudy, M. and M. D. Zoback, Compressive and tensile failure of boreholes arbitrarily-inclined to principal stress axes: Application to the KTB boreholes, Germany, *Int. J. Rock. Mech. Min. Sci.*, *30*, 1035–1038, 1993.
- Brudy, M. and M. D. Zoback, Drilling-induced tensile wall-fractures: Implications for determination of *in situ* stress orientation and magnitude, *Int. J. Rock. Mech. Min.*

- Sci.*, 36, 191–215, 1999.
- Brudy, M., M. D. Zoback, K. Fuchs, F. Rummel, and J. Baumgärtner, Estimation of the complete stress tensor to 8 km depth in the KTB scientific drill holes: Implications for crustal strength, *J. Geophys. Res.*, 102, 18,453–18,475, 1997.
- Byerlee, J. D., Friction of rocks, *Pure Appl. Geophys.*, 116, 615–626, 1978.
- Carey, E. and B. Brunier, Analyse théorique et numérique d'un modèle mécanique élémentaire appliqué à l'étude d'une population de failles, *C.R. Acad. Sci. Paris.*, 279, 891–894, 1974.
- Carey-Gailhardis, E. and J. L. Mercier, A numerical method for determining the state of stress using focal mechanisms of earthquake populations: application to Tibetan teleseisms and microseismicity of Southern Peru, *Earth Planet. Sci. Lett.*, 82, 165–179, 1987.
- Cheatham, J., A new hypothesis to explain stability of borehole breakouts, *Int. J. Rock Mech. Min. Sci.*, 30, 1095–1101, 1993.
- Cornet, F. H. and B. Valette, In situ stress determination from hydraulic injection test data, *J. Geophys. Res.*, 89, 11,527–11,537, 1984.
- Coulomb, C. A., Sur une application des règles de Maximis et Minimis a quelques problèmes de statique relatifs à l'Architecture, *Acad. Roy. des Sciences Memoires de math. et de physique par divers savans*, 7, 343–382, 1773.
- Dart, R. and M. L. Zoback, Well-bore breakout-stress analysis within the continental United States, in *Proc. 2nd Int. Symp. on Borehole Geophysics for Minerals, Geotechnical, and Groundwater Applications*, pp. 1–11, Soc. of Prof. Well Log Analysts Publ., Golden, USA, 1985.
- DeMets, C., R. Gordon, D. Argus, and S. Stein, Effect of recent revisions to the magnetic reversal time scale on estimates of current plate motions, *Geophys. Res. Lett.*, 21, 2191–2194, 1994.
- Einarsson, P., Earthquakes and present-day tectonism in Iceland, *Tectonophysics*, 189, 261–279, 1991.
- Ekstrom, M., C. Dahan, M. Chen, P. Lloyd, and D. Rossi, Formation imaging with microelectrical scanning arrays, *Log Anal.*, 28, 294–306, 1987.
- Etchecopar, A., G. Vasseur, and M. Daignieres, An inverse problem in microtectonics for the determination of stress tensors from fault striation analysis, *J. Struct. Geol.*, 3, 51–65, 1981.
- Fairhurst, C., Methods of determining the in situ rock stresses at great depths, Technical report, Mo. River Div. Corps of Eng., Omaha, Nebr., TRI-68, 1968.
- Gephart, J. W., Principal stress directions and the ambiguity in fault plane identification from focal mechanisms, *Bull. Seismol. Soc. Am.*, 75, 621–625, 1985.
- Gephart, J. W., FMSI: A FORTRAN program for inverting fault/slickenside and earthquake focal mechanism data to obtain the regional stress tensor, *Comp. Geosci.*, 16, 953–989, 1990.
- Gephart, J. W. and D. W. Forsyth, An improved method for determining the regional stress tensor using earthquake focal mechanism data: Application to the San Fernando earthquake sequence, *J. Geophys. Res.*, 89, 9305–9320, 1984.
- Goldstein, H., *Classical Mechanics*, Addison-Wesley Publishing Company, Reading, Massachusetts, second edition, 1980.
- Gough, D. and J. Bell, Stress orientation from borehole wall fractures with examples

- from Colorado, East Texas, and northern Canada, *Can. J. Earth Sci.*, *19*, 1358–1370, 1982.
- Guðmundsson, Á., Ocean-ridge discontinuities in Iceland, *J. Geol. Soc. London*, *152*, 1011–1015, 1995.
- Gustafsson, G. and I. Rhén, DDP evaluation of hydrogeological data, Sector Report, Deep Gas Research Project U(G) 1990/48, Vattenfall Utvecklings AB, Älvkarleby, Sweden, 1990.
- Haimson, B. and C. Fairhurst, Initiation and extension of hydraulic fractures in rock, *Soc. Petrol. Eng. J.*, pp. 310–318, Sept., 1967.
- Haimson, B. and C. Fairhurst, In situ stress determination at great depth by means of hydraulic fracturing, in *Proc. 11th US Symp. Rock Mech.*, pp. 559–584, SME/AIME, Berkeley, 1970.
- Haimson, B. and I. Song, Laboratory study of borehole breakouts in Cordova Cream: a case of shear failure mechanism, *Int. J. Rock. Mech. Min. Sci.*, *30*, 1047–1056, 1993.
- Hiramatsu, Y. and Y. Oka, Stress around a shaft or level excavated in ground with a three-dimensional stress state, *Mem. Fac. Eng. Kyoto Univ.*, *XXIV(I)*, 56–76, 1962.
- Horiuchi, S., G. Rocco, and A. Hasegawa, Discrimination of fault planes from auxiliary planes based on simultaneous determination of stress tensor and a large number of fault plane solutions, *J. Geophys. Res.*, *100*, 8327–8338, 1995.
- Hubbert, K. and D. Willis, Mechanics of hydraulic fracturing, *Petrol. Trans. AIME, T.P. 4597, 210*, 153–166, 1957.
- Jaeger, J. C. and N. W. G. Cook, *Fundamentals of Rock Mechanics*, Chapman and Hall, New York, third edition, 1979.
- Julian, B. R., A. D. Miller, and G. R. Foulger, Non-double-couple earthquakes, 1, Theory, *Rev. Geophys.*, *36*, 525–549, 1998.
- Kirsch, G., Die Theorie der Elastizität und die Bedürfnisse der Festigkeitslehre, *Zeit. Ver. dt. Ingenieure*, *42*, 797–807, 1898.
- Lee, M. and B. Haimson, Laboratory study of borehole breakouts in Lac du Bonnet granite: A case of extensile failure mechanism, *Int. J. Rock. Mech. Min. Sci.*, *30*, 1039–1045, 1993.
- Magee, M. E., *Crustal stress state inferred from earthquake focal mechanisms: Recognition of a non-uniform stress state, slip plane selection criteria and implications for the mechanics of faulting*, Ph.D. thesis, Stanford Univ., Stanford, Calif., USA, 1997.
- Mastin, L., Effect of borehole deviation on breakout orientations, *J. Geophys. Res.*, *93*, 9187–9195, 1988.
- McKenzie, D. P., The relation between fault plane solutions for earthquakes and the directions of the principal stresses, *Bull. Seismol. Soc. Am.*, *59*, 591–601, 1969.
- Michael, A. J., Determination of stress from slip data: Faults and folds, *J. Geophys. Res.*, *89*, 11517–11526, 1984.
- Michael, A. J., Use of focal mechanisms to determine stress: A control study, *J. Geophys. Res.*, *92*, 357–368, 1987.
- Moos, D. and M. D. Zoback, Utilization of observations of wellbore failure to constrain the orientation and magnitude of crustal stresses: Application to continental, Deep Sea Drilling Project and Ocean Drilling Program boreholes, *J. Geophys. Res.*, *95*, 9305–9325, 1990.
- Müller, B., V. Wehrle, and K. Fuchs, The 1997 release of the World Stress Map (available

- on-line at <http://www-wsm.physik.uni-karlsruhe.de/pub/rel97/wsm97.html>), 1997.
- Nagel, R., *Das Spannungsfeld in der Geothermiebohrung Soultz-sous-Forêts abgeleitet aus vertikalen Strukturen in einer Tiefe von 1.9 bis 3.6 km*, Master's thesis, Universität Karlsruhe, in German, 1994.
- Passerini, P., M. Marcucci, G. Sguazzoni, and E. Pecchioni, Longitudinal strike-slip faults in oceanic rifting: A mesostructural study from western to southeastern Iceland, *Tectonophysics*, *269*, 65–89, 1997.
- Peška, P. and M. D. Zoback, Compressive and tensile failure of inclined well bores and determination of in situ stress and rock strength, *J. Geophys. Res.*, *100*, 12,791–12,811, 1995.
- Plumb, R. and S. H. Hickman, Stress-induced borehole elongation: A comparison between the four-arm dipmeter and the borehole televiewer in the Auburn geothermal well, *J. Geophys. Res.*, *90*, 5513–5521, 1985.
- Qian, W. and L. B. Pedersen, Inversion of borehole breakout orientation data, *J. Geophys. Res.*, *96*, 20,093–20,107, 1991.
- Reches, Z., Determination of the tectonic stress tensor from slip along faults that obey the Coulomb yield condition, *Tectonics*, *6*, 849–861, 1987.
- Reid, H. F., *The California earthquake of April 18, 1906: Report of the State Earthquake Investigation Commission*, vol. II, *The Mechanics of the Earthquake*, Carnegie Inst. of Washington, Washington, D.C., 1910.
- Rögnvaldsson, S. T. *et al.*, Skjálftahrina í Ölfusi í nóvember 1998, Technical Report VÍ-G98046-JA09, Icelandic Meteorol. Off., Reykjavík, Iceland, (in Icelandic), 1998.
- Rögnvaldsson, S. T. and R. Slunga, Routine fault plane solutions for local networks: A test with synthetic data, *Bull. Seismol. Soc. Am.*, *83*, 1232–1247, 1993.
- Sæmundsson, K., Hengill, jarðfræðikort (berggrunnur) 1:50000, Orkustofnun, Hitaveita Reykjavíkur og Landmælingar Íslands, Reykjavík, Iceland, Geological map, 1995.
- Schmitt, D. and M. D. Zoback, Poroelastic effects in the determination of the maximum horizontal principal stress in hydraulic fracturing tests – a proposed breakdown equation employing a modified effective stress relation for tensile failure, *Int. J. Rock Mech. Min. Sci.*, *26*, 499–506, 1989.
- Scholz, C. H., *The mechanics of earthquakes and faulting*, Cambridge University Press, Cambridge, 1990.
- Shamir, G. and M. D. Zoback, Stress orientation profile to 3.5 km depth near the San Andreas fault at Cajon Pass, California, *J. Geophys. Res.*, *97*, 5059–5080, 1992.
- Shomali, H. and R. Slunga, Body wave moment tensor inversion of local earthquakes: An application to the South Iceland Seismic Zone, *Geophys. J. Int.*, *140*, 63–70, 2000.
- Sigmundsson, F., P. Einarsson, R. Bilham, and E. Sturkell, Rift–transform kinematics in south Iceland: Deformation from Global Positioning System measurements, 1986 to 1992, *J. Geophys. Res.*, *100*, 6235–6248, 1995.
- Slunga, R., Earthquake source mechanism determination by use of body–wave amplitudes – an application to Swedish earthquakes, *Bull. Seismol. Soc. Am.*, *71*, 25–35, 1981.
- Slunga, R., P. Norrmann, and A.-C. Glans, Baltic shield seismicity, the results of a regional network, *Geophys. Res. Lett.*, *11*, 1247–1250, 1984.
- Slunga, R., S. T. Rögnvaldsson, and R. Böðvarsson, Absolute and relative locations of similar events with application to microearthquakes in southern Iceland, *Geophys. J. Int.*, *123*, 409–419, 1995.

- Stefánsson, R., R. Böðvarsson, R. Slunga, P. Einarsson, S. Jakobsdóttir, H. Bungum, S. Gregersen, J. Havskov, J. Hjelme, and H. Korhonen, Earthquake Prediction Research in the South Iceland Seismic Zone and the SIL Project, *Bull. Seismol. Soc. Am.*, *83*, 696–716, 1993.
- Tenzer, H., L. Mastin, and B. Heinemann, Determination of planar discontinuities and borehole geometry in the crystalline rock of borehole GPK1 at Soult-sous-Forêts, in *Geothermal science and technology*, edited by Bresee, pp. 31–68, Gordon and Breach Publishers, 1994.
- Tryggvason, K., E. Huseby, and R. Stéfansson, Seismic image of the hypothesized Icelandic hot spot, *Tectonophysics*, *100*, 97–118, 1983.
- Vasseur, G., A. Etchecopar, and H. Philip, Stress state inferred from multiple focal mechanisms, *Ann. Geophys.*, *1*, 291–298, 1983.
- Vernik, L. and M. D. Zoback, Estimation of maximum horizontal principal stress magnitude from stress-induced well bore breakouts in the Cajon Pass scientific research borehole, *J. Geophys. Res.*, *97*, 5109–5119, 1992.
- Wallace, R. E., Geometry of shearing stress and relation to faulting, *J. Geol.*, *59*, 118–130, 1951.
- Wessel, P. and W. H. F. Smith, New, improved version of Generic Mapping Tools released, *Eos Trans., AGU*, *79*, 579, 1998.
- Wiebols, G. and N. Cook, An energy criterion for the strength of rock in polyaxial compression, *Int. J. Rock. Mech. Min. Sci.*, *5*, 529–549, 1968.
- Zemanek, J., E. Glenn, L. Norton, and R. Caldwell, Formation evaluation by inspection with the borehole televiewer, *Geophysics*, *35*, 254–269, 1970.
- Zheng, Z., J. Kemeny, and N. Cook, Analysis of borehole breakouts, *J. Geophys. Res.*, *94*, 7171–7182, 1989.
- Zoback, M. D. and G. C. Beroza, Evidence for near-frictionless faulting in the 1989 (M 6.9) Loma Prieta, California, earthquake and its aftershocks, *Geology*, *21*, 181–185, 1993.
- Zoback, M. D. and J. Healy, In situ stress measurements to 3.5 km depth in the Cajon Pass scientific research borehole: Implications for the mechanics of crustal faulting, *J. Geophys. Res.*, *97*, 5039–5057, 1992.
- Zoback, M. D., D. Moos, L. Mastin, and R. Andersson, Wellbore breakouts and in situ stress, *J. Geophys. Res.*, *90*, 5523–5530, 1985.
- Zoback, M. D. and M. L. Zoback, Tectonic stress field of North America and relative plate motions, in *Neotectonics of North America, Decade Map*, vol. 1, edited by M. Z. D.B. Slemmons, E.R. Engdahl and M. Blackwell, pp. 339–366, Geol. Soc. Am., Boulder, CO, USA, 1991.
- Zoback, M. L., First- and second-order patterns of stress in the lithosphere: The World Stress Map project, *J. Geophys. Res.*, *97*, 11,703–11,728, 1992.
- Zoback, M. L. *et al.*, Global patterns of tectonic stress, *Nature*, *341*, 291–298, 1989.
- Zoback, M. L. and M. D. Zoback, State of stress in the conterminous United States, *J. Geophys. Res.*, *85*, 6113–6156, 1980.
- Zoback, M. L. and M. D. Zoback, Tectonic stress field of the conterminous United States, *Mem. Geol. Soc. Am.*, *172*, 523–539, 1989.

A Computer programs

A large fraction of my PhD studies was spent implementing the methods and algorithms described in papers II and III of this thesis. This coding effort has resulted in the two computer programs `sti`, for the stress tensor inversion, and `ampcorr`, spectral amplitude correlation. The programs will not be listed here, they comprise of approximately 10000 lines of code (`wc -l` reports 11450 but I estimate that 10% are comments and then there are a couple of blank lines as well). The programs will, however, be publicly available as soon as I have made them a little more comprehensible. In addition to the main programs I worked with Sigurður Rögnvaldsson on a C library of I/O routines for the SIL system, with Sigurður Rögnvaldsson and Ragnar Slunga on a C version of Ragnar's focal mechanism routines, and with Reynir Bððvarsson on utility routines for the SIL data acquisition system.

A.1 `sti`

The stress tensor inversion program `sti` implements the ideas that was presented in paper II. The program is written entirely in C and includes library functions for vector and matrix manipulation, angular conversion between different focal mechanism conventions and the stress estimation routines. Input data are taken either from the SIL data base or from a program native format, obtainable by the utility program `conv2sti`. The grid size can be chosen between increments of 2° to 20° , with R in increments of 0.05 or 0.1. Output data are in the form of ASCII files with information on the estimated state of stress, confidence limits and chosen fault planes. I have a number of GMT (Generic Mapping Tool) [Wessel and Smith, 1998] scripts for the visualization of the results.

```
thor:~/sil/rst> sti -h
```

```
STRESS TENSOR INVERSION OF EARTHQUAKE FOCAL MECHANISMS
```

```
sti [-h] data file [-c config file][-d num] [-f #] [-l #] [-n]
    [-o output file name] [-s]
```

```
The program inverts earthquake focal mechanisms or geologic
fault slip data for the stress tensor that caused the movement on
the faults.
```

```
The inversion process is described in Lund and Slunga, JGR, 1999.
```

```
For optimal use of the program's error messages, run the program as:
sti data_file [options] >& data_file.err &
```

```
data file      The program accepts input data either in SIL format,
```

a *.grx or *.grs file, or in a program native format.
The native format can be obtained from strike,dip and rake data with the program conv2sti.

Options:

- c Configuration file with other name than rst.conf or in another directory. Default is rst.conf in the current directory.
- d Dump SIL data into other formats:
 - 1 A total dump in sti native format.
 - 2 Dump optimal planes in Gephart & Forsyth #7
 - 3 Dump final planes in Gephart & Forsyth #7
- f First event in inversion. Number in list of approved events, default is 1.
- h This text.
- l Last event in inversion. Number in list of approved events, default is last.
- n Write a file with the non-redundant events as defined by the gridding of Magee, 1997
- o Base name for output files. Default is the input file name extended with the inversion method
- s Read in the events and write out relevant info, then exit.

Bjorn Lund, November 1996. Version 1.4, BL June 1999.

A.2 ampcorr

The spectral amplitude correlation described in paper III is implemented in program ampcorr. The program is written entirely in C and includes the linear cross-correlation algorithm from Numerical Recipes in C. Input data are spectral amplitudes from the SIL data base. Output is in ASCII format with tables of dates, number of solitary events and number of groups, plus a variety of alternatives for output of correlation matrices and groups.

```
thor:~/sil/amp> ampcorr -h
```

SPECTRAL AMPLITUDE CORRELATION.

Group events according to the correlation of their spectral amplitudes in order to find events with similar focal mechanisms.
The algorithm is described in Lund and Bodvarsson, submitted to BSSA, 1999.

```
ampcorr [-h] [-1|2|3] [-a] [-b] [-c conf_file] [-d 4] [-f] [-g] [-i #]
        [-j #] [-m #] [-n #] [-o outfile] [-r lat1 lat2 lon1 lon2 dep1
        dep2 time1 time2] [grx_file]
```

- 1|2|3 Mode of operation. Has to be indicated, except with -a or -d.
 - 1 Correlate all events with all others at once.
 - 2 Correlate all events, one by one, in a single batch.
 - 3 Make batches of reduced events.

General options:

- a Create a generic config file called New_ampcorr.cf.
- c Name of the config file. Default is ampcorr.cf.
- d 4 Dump a grx file containing the usable events.
- f Use phase logs as amplitude input. Default is ome.
- h This text.
- j Jump over the first # reduced events in the grx file.
- o Base name for output files. Default is the input file name.
- r Correlate events within the specified space-time period.
Lat, lon in decimal degrees, dep in km and time as
1999 03 07 18 14 30

Mode 1 options:

- b Write only the best event in each group in the grx file.
Default is all events.
- g Write separate grx files for all groups. Default is one common.

Mode 2 options:

- i Initial number of events to be read. Default is 20.
- m Number of events in the correlation memory. If used with -t,
number of days. Default is the entire list.
- t Use number of days for correlation memory (-m).
Default is number of events.

Mode 3 options:

- n Number of reduced events in each grx output batch. Use
even number. Default is 50.

Bjorn Lund, April 1999. Version 1.3, BL January 2000.